

# Shapley Supercluster Survey: ram-pressure stripping versus tidal interactions in the Shapley supercluster

P. Merluzzi,<sup>1★</sup> G. Busarello,<sup>1★</sup> M. A. Dopita,<sup>2,3★</sup> C. P. Haines,<sup>4,5</sup> D. Steinhauser,<sup>6</sup>  
H. Bourdin<sup>7,8</sup> and P. Mazzotta<sup>7</sup>

<sup>1</sup>INAF-Osservatorio Astronomico di Capodimonte, Via Moiariello 16, I-80131 Napoli, Italy

<sup>2</sup>Research School of Astronomy and Astrophysics, Australian National University, Cotter Rd., Weston ACT 2611, Australia

<sup>3</sup>Astronomy Department, Faculty of Science, King Abdulaziz University, PO Box 80203, Jeddah, Saudi Arabia

<sup>4</sup>Departamento de Astronomía, Universidad de Chile, Casilla 36-D, Correo Central, Santiago, Chile

<sup>5</sup>INAF-Osservatorio Astronomico di Brera, Via Brera 28, I-20121 Milano, Italy

<sup>6</sup>Institute of Astro- and Particle Physics, University of Innsbruck, Technikerstr. 25, A-6020 Innsbruck, Austria

<sup>7</sup>Dipartimento di Fisica, Università di Roma Tor Vergata, Via della Ricerca Scientifica 1, I-00133 Roma, Italy

<sup>8</sup>Harvard-Smithsonian Center for Astrophysics, 60 Garden St, Cambridge, MA 02138, USA

Accepted 2016 May 15. Received 2016 May 13; in original form 2016 February 19

## ABSTRACT

We present two new examples of galaxies undergoing transformation in the Shapley supercluster core. These low-mass ( $M_{\star} \sim 0.4\text{--}1 \times 10^{10} M_{\odot}$ ) galaxies are members of the two clusters SC 1329–313 ( $z \sim 0.045$ ) and SC 1327–312 ( $z \sim 0.049$ ). Integral-field spectroscopy complemented by imaging in the *ugriK* bands and in H $\alpha$  narrow band is used to disentangle the effects of tidal interaction (TI) and ram-pressure stripping (RPS). In both galaxies, SOS 61086 and SOS 90630, we observe one-sided extraplanar ionized gas extending respectively  $\sim 30$  and  $\sim 41$  kpc in projection from their discs. The galaxies' gaseous discs are truncated, and the kinematics of the stellar and gas components are decoupled, supporting the RPS scenario. The emission of the ionized gas extends in the direction of a possible companion for both galaxies suggesting a TI. The overall gas velocity field of SOS 61086 is reproduced by ad hoc *N*-body/hydrodynamical simulations of RPS acting almost face-on and starting  $\sim 250$  Myr ago, consistent with the age of the young stellar populations. A link between the observed gas stripping and the cluster–cluster interaction experienced by SC 1329–313 and A3562 is suggested. Simulations of ram pressure acting almost edge-on are able to fully reproduce the gas velocity field of SOS 90630, but cannot at the same time reproduce the extended tail of outflowing gas. This suggests that an additional disturbance from a TI is required. This study adds a piece of evidence that RPS may take place in different environments with different impacts and witnesses the possible effect of cluster–cluster merger on RPS.

**Key words:** galaxies: clusters: general – galaxies: clusters: individual: SC 1327–312 – galaxies: clusters: individual: SC 1329–313 – galaxies: evolution – galaxies: photometry – galaxies: stellar content.

## 1 INTRODUCTION

The evolution of galaxies depends both on their intrinsic properties, such as their mass, and external ‘accidents’ in which the galaxies are randomly involved during their life. These external events include tidal interactions (TIs), galaxy mergers, ram-pressure and viscous stripping, evaporation and ‘starvation’ (Gunn & Gott 1972; Toomre & Toomre 1972; Cowie & Songalia 1977; Larson, Tinsley & Caldwell 1980; Nulsen 1982; Byrd & Valtonen 1990; Barnes &

Hernquist 1991; Moore et al. 1996; Bekki 2001). Together, these events serve to transform galaxies by disturbing their kinematics, depleting their reservoirs of gas, and so quenching star formation (SF). The time-scales and efficiencies of such mechanisms are different and depend on both the properties of the galaxies and on their environment (for a review see Boselli & Gavazzi 2006). In particular, within the crowded and dense environments of galaxy clusters and groups, the probability that hydrodynamical events transform galaxies increases significantly. This may serve to explain the origin of the different galaxy populations observed in clusters and field in the local Universe (e.g. Dressler 1980; Lewis et al. 2002; Bamford et al. 2009).

\* E-mail: merluzzi@na.astro.it (PM); gianni@na.astro.it (GB); michael.dopita@anu.edu.au (MAD)

In this work, we investigate the possibility of disentangling two mechanisms which have been invoked as main drivers in transforming spiral galaxies into S0s and dEs: ram-pressure stripping (RPS; Gunn & Gott 1972; Abadi, Moore & Bower 1999) and galaxy–galaxy TIs (Toomre & Toomre 1972; Moore et al. 1996).

Galaxies orbiting into a cluster feel the ram pressure exerted by the hot and dense intracluster medium (ICM) which can effectively remove the cooler interstellar medium (ISM) in the galaxy starting from outside and thus quenching SF in the ram-pressure stripped regions. The time-scale for RPS is about one cluster crossing time ( $\sim 10^9$  yr). As emphasized by Gunn & Gott (1972), this cluster-specific mechanism efficiently depletes the gas of massive spiral galaxies only within the cluster cores where the dense ICM is expected to be located. However, the effects of ram pressure depend on both galaxy and ICM properties and may easily extend to poorer environments for low-mass galaxies (Marcolini, Brighenti & D’Ercole 2003), and not only for them. Using hydrodynamical cosmological simulations, Bahé et al. (2013) investigated the increase of gas content and SF in cluster galaxies with the clustercentric distance. They found that this observed large-scale trend, approaching the values of the field galaxy sample only at  $\sim 5r_{200}$ , can be explained by a combination of (i) ‘pre-processing’ of galaxies within infalling groups; (ii) ‘overshooting’ for those galaxies that are not falling in for the first time; and (iii) RPS. Simulations of ongoing RPS show that such a mechanism not only severely truncates the gas disc of  $L^*$  galaxies in high-density environments, but also in low-density environments, where moderate ram pressures are foreseen, their gas disc may be disturbed and bent (Roediger & Hensler 2005). Observations of special events of gas stripping confirmed that RPS is acting more efficiently than previously postulated by Gunn & Gott (1972), playing a role also outside the cluster cores (e.g. Chung et al. 2007; Merluzzi et al. 2013).

Ram pressure may also compress and shock the ISM, temporarily enhancing the SF in the inner disc as well as in the stripped gas (Byrd & Valtonen 1990; Fujita & Nagashima 1999; Tonnesen & Bryan 2012; Bekki 2014). These effects are observed in a few cases (Merluzzi et al. 2013; Ebeling, Stephenson & Edge 2014; Kenney et al. 2014). Since it is highly effective in quenching the SF, RPS is also considered to be one of the most important processes, although not the only one, to convert spirals and irregulars into S0 and spheroidal galaxies (see Kormendy & Bender 2012).

A counter-argument to this hypothesis is that S0s differ from normal spirals by their higher bulge luminosities rather than simply having fainter discs (Christlein & Zabludoff 2004), and this is not explained with the RPS or starvation mechanisms. Other mechanisms such as TIs (merging, fly-bys; Toomre & Toomre 1972) and harassment (which is also a TI in a wider sense; Moore et al. 1996) are better capable of channelling material on to a central bulge, sufficient to produce the higher central mass densities seen in cluster spirals and ultimately the stellar phase densities found in S0s (Moran et al. 2007). In general, TIs gravitationally perturb the gas and stellar components, trigger central starbursts and strip stars and gas from the disc of the involved spiral galaxies producing tails and bridges (see Toomre & Toomre 1972; Larson & Tinsley 1978; Kennicutt & Keel 1984; Keel et al. 1985; Barnes & Hernquist 1991, 1992, 1996; Woods, Geller & Barton 2006).

In cluster environments, due to the high relative velocities of the colliding galaxies, TI time-scales are shorter ( $\sim 10^8$  yr) than in the field, and a single passage may only marginally affect the dynamics of their stellar populations. The geometry of the encounter and the relative galaxy properties are important parameters in determining the size of the dynamical perturbation. Multiple

encounters (harassment) – which are of course more common in clusters – are probably necessary to substantially perturb the stellar content.

The presence of both gas and stars outside the galaxy disc may arise from either RPS or through TIs. Although each mechanism will produce distinctive distributions in the extraplanar gas and stars, it may be not straightforward to distinguish which process is acting on a particular galaxy because projection effects may mask the geometries of the outflowing matter (e.g. Bournaud et al. 2004; Roediger & Brüggen 2006). The internal kinematics can help to distinguish between these mechanisms; while the gas component suffers the ram pressure which is able to modify its velocity field, the stellar kinematics will be affected only in the case of TIs.

Most, if not all, of these observables are transient phenomena. After  $\sim 1$  Gyr, the ‘memory’ of either the RPS or TI is washed out (see Kronberger et al. 2006; Oh et al. 2008). The permanent results are (i) the SF quenching, achieved with both mechanisms, although on different time-scales; (ii) the truncation of the gaseous discs by RPS; (iii) the structural modification by TIs. Each galaxy can be involved in different ‘accidents’ across cosmic time, making it extremely difficult to understand which mechanism really prevails in transforming the star-forming disc galaxies accreted from the field into the S0 and dE populations which now dominate cluster cores.

To address the challenge of understanding the physics of galaxy transformations, we need integral-field spectroscopy (IFS). IFS allows us to resolve the different spatial components in the galaxies, and so measure the dynamical disturbance of the stellar component, discover disturbed gas velocity fields, determine the local enhancement and spatial trend of the SF, and to use chemical abundance analysis to identify the source of the extraplanar gas.

With this in mind, we have undertaken IFS observations with the Wide-Field Spectrograph (WiFeS; Dopita et al. 2007, 2010) of a small but carefully selected galaxy sample in the Shapley supercluster core (SSCC), drawn from the Shapley Supercluster Survey (ShaSS; Merluzzi et al. 2015) which aims to investigate the role of the mass assembly on galaxy evolution. It covers  $23 \text{ deg}^2$  centred on the SSCC with ESO-VLT Survey Telescope (VST) *ugri* and ESO-Visible and Infrared Survey Telescope for Astronomy (VISTA) *K*-band imaging. The Shapley supercluster is located at a redshift  $z \sim 0.05$ , and represents the most dynamically active and dense structure in the local Universe. Thus, the probability to observe evidence of environmental effects on galaxy evolution is dramatically enhanced. The targets for the IFS have been selected from the spectroscopic catalogue of ShaSS which is 80 per cent complete down to  $i = 17.6$  ( $m^* + 3$ ). All these galaxies are supercluster members, resolved in the optical images and display (i) disturbed morphologies, such as asymmetry and tails; (ii) hints of extraplanar emission; (iii) evidence of star-forming knots. About 80 galaxies satisfy at least two of these properties. After this *visual* selection, the galaxies are targeted with a 45 min exposures of WiFeS which allow us to ascertain which of them actually present extraplanar emission and then become the high-priority targets in our investigation. At present, 17 supercluster galaxies have been observed. They belong to different environments, from dense cluster cores to the regions where cluster–cluster interactions are taking place, and out to the much less populated areas.

In our first study (Merluzzi et al. 2013), we identified a bright ( $L > L^*$ ) barred spiral galaxy (SOS 114372)  $\sim 1$  Mpc from the centre of the rich cluster A3558 in the SSCC, which is being affected by RPS. IFS observations revealed ongoing gas stripping in the

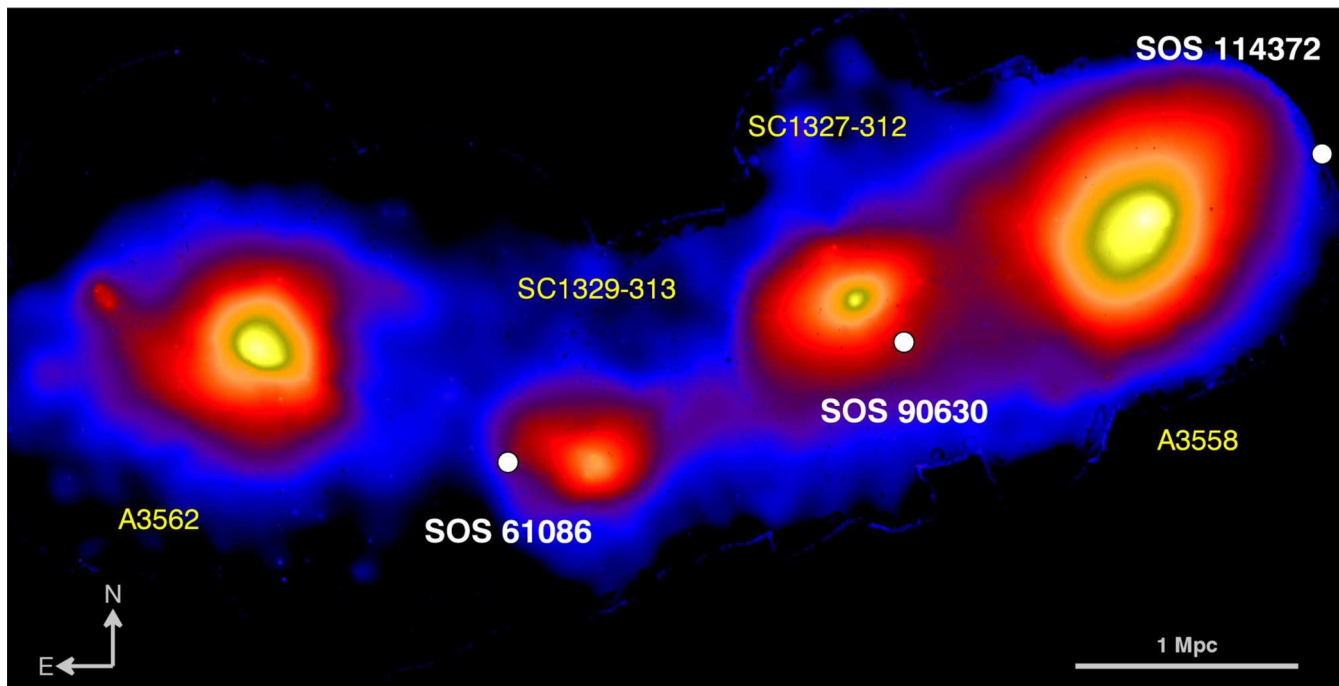


**Figure 1.** The positions of SOS 61086 and SOS 90630 (white dots) are indicated on the X-ray emission map including four out of five clusters of the SSCC. The position of SOS 114372 (see the text) is also marked. The X-ray surface brightness is derived from a wavelet analysis of *XMM-Newton* images extracted in the 0.5–2.5 keV energy band, which have been corrected for spatially variable effective exposure and background components. Scale and orientation are shown at the bottom.

form of one-sided extraplanar ionized gas along the full extent of the disc, simultaneously with a starburst triggered by gas compression along the leading edge of the galaxy. The galaxy is subjected to weak–moderate ram pressure, as defined by Roediger & Hensler (2005). This adds a piece of evidence to the fact that RPS is acting more efficiently on the galaxy ISM than previously foreseen and also outside of the cluster cores, as also observed in the Virgo cluster by Chung et al. (2009). This is possibly the principal transformation process quenching SF in spirals, although certainly it is helped by other processes affecting the structure of the galaxies.

In this work, we present the results for the galaxies SOS 61086 and SOS 90630. These two galaxies are 2.9 and 2.3 *K*-band mag fainter with respect to SOS 114372 allowing us to extend the investigation of the environmental effects to a lower stellar mass range, but also to investigate different environments, since both are members of low-mass clusters ( $\mathcal{M}_{\text{cl}} \sim 10^{14} M_{\odot}$ ) involved in interactions.

In Section 2, the main properties of the targets are presented. Observations and data reduction are described in Sections 3 and 4. The data analysis is summarized in Section 5. The results are given in Sections 6 and 7 for the two galaxies. In Section 8, we discuss the possible origins of the observed extraplanar gas, and in Section 9 we compare the observed gas velocity field with those derived from hydrodynamical simulations and discuss possible drivers for the observed transformations. Our conclusions are summarized in Section 10.

Throughout the paper, and in common with the other papers of this series, we adopt a cosmology with  $\Omega_{\text{M}}=0.3$ ,  $\Omega_{\Lambda}=0.7$  and  $H_0=70 \text{ km s}^{-1} \text{ Mpc}^{-1}$ . According to this cosmology, 1 arcsec corresponds to 0.880 kpc at  $z=0.0447$  (SC 1329–313) and 0.966 kpc at  $z=0.0493$  (SC 1327–312). Velocities and velocity dispersions are given accounting for the relativistic correction.

## 2 THE GALAXIES

The galaxies SOS 61086 and SOS 90630, named following the Shapley Optical Survey (SOS) identification<sup>1</sup> (Haines et al. 2006; Mercurio et al. 2006), are spiral galaxies respectively 2.7 and 2.1 mag fainter than  $m^*$  in the *K* band ( $K^* = 11.7$  at the supercluster redshift; Merluzzi et al. 2010) and with stellar masses  $\mathcal{M}_* \sim 0.4 \times 10^{10} M_{\odot}$  and  $\mathcal{M}_* \sim 1 \times 10^{10} M_{\odot}$ . Both lie in poor cluster environments, as indicated in Fig. 1 (white dots) relative to the SSCC as traced by the X-ray surface brightness derived by *XMM-Newton* images in the 0.5–2.5 keV energy band (see Section 8.3.1).

### 2.1 SOS 61086

This galaxy has a redshift  $z = 0.04261$  ( $V_h = 12502 \text{ km s}^{-1}$ ) and is located at 282 kpc in projection from the X-ray centre of the cluster SC 1329–313 ( $\mathcal{M}_{\text{cl}} \sim 3.7 \times 10^{14} M_{\odot}$ ; Ragone et al. 2006) in the SSCC. SC 1329–313 forms a well-defined, distinct structure both spatially and in velocity space. The distribution of galaxies and the X-ray emission are both elongated along the ENE direction towards Abell 3562 (see also Finoguenov et al. 2004; Giacintucci et al. 2005). By analysing the caustic diagram of the ShaSS spectroscopic sample (Haines et al., in preparation), we determine its mean recession velocity of  $13114 \text{ km s}^{-1}$  ( $z = 0.04475$ ), with a velocity dispersion of just  $348 \pm 28 \text{ km s}^{-1}$ , based on 55 member galaxies within  $r_{200}$  (0.86 Mpc; see also Bardelli et al. 1998b). Both dominant elliptical galaxies have very similar recession velocities ( $12807$  and  $12758 \text{ km s}^{-1}$ ), which are  $300\text{--}350 \text{ km s}^{-1}$  lower

<sup>1</sup> In the ShaSS survey (Merluzzi et al. 2015), they correspond to the galaxies ShaSS403015754 and ShaSS408053848, respectively (Mercurio et al. 2015).



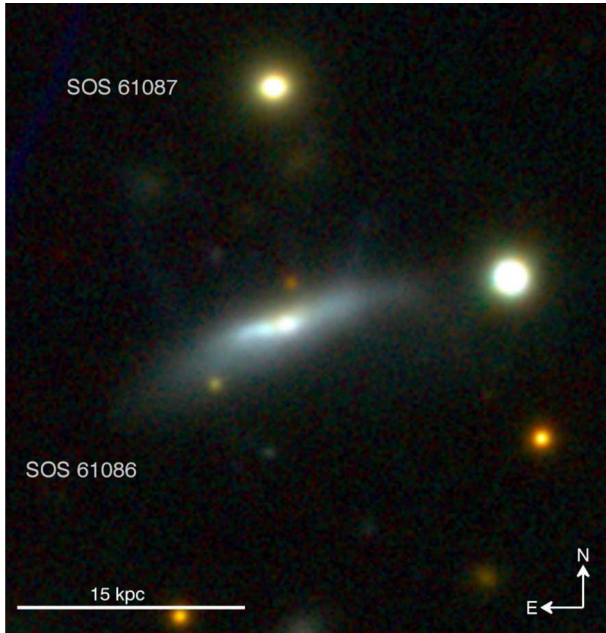


**Figure 2.** Composite *gri* image of the field including SOS 61086 in the centre and SOS 61087 located north.

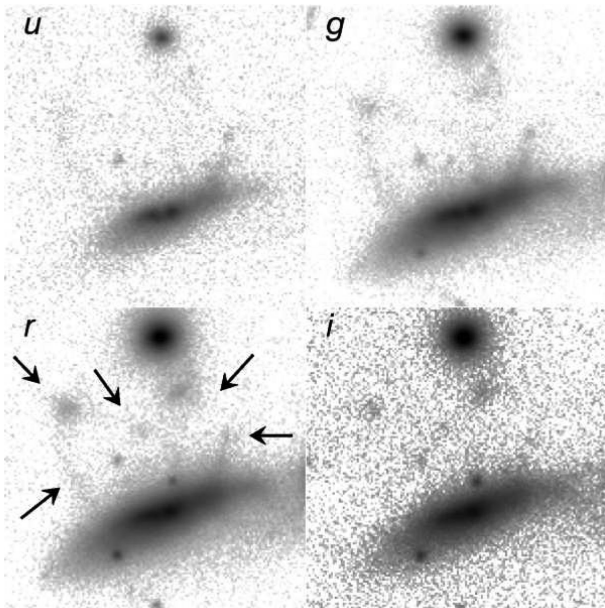


**Figure 3.** Detail of the field of Fig. 2 shown in the *ugri* bands, with hints of (low-brightness) extraplanar material highlighted by the arrows on the *r*-band image.

than the mean. This suggests that the line-of-sight (LOS) peculiar velocity of SOS 61086 with respect to the main group is about  $-600 \text{ km s}^{-1}$ .

A *gri* composite image of the galaxy, derived from the optical imaging of ShaSS, is shown in Fig. 2. The pixel scale of the imaging is  $0.214 \text{ arcsec pixel}^{-1}$  with a seeing less than  $0.8 \text{ arcsec}$  in the *gr* bands and  $\sim 0.9 \text{ arcsec}$  in the *i* band. Fig. 2 shows SOS 61086 in the field centre and another cluster member, SOS 61087, at about  $17 \text{ kpc}$  to the north. The bright source to the right of SOS 61086 is a star. Fig. 3 shows part of the field of Fig. 2 in the four VST bands *ugri*. It focuses on the area where hints of extraplanar material are present

(highlighted by the arrows in the *r*-band image). These figures show hints of matter beyond the stellar disc in the northerly direction with respect to SOS 61086. In particular, two faint filaments leading NW and NE from the disc few kiloparsecs in projection from the galaxy centre. The extraplanar emission seems to form a fan-like structure bordered by the two filaments. Two faint clumps located NW and NE with respect to the galaxy centre and out of the disc can be also distinguished. It is not clear if these clumps are associated with the galaxy, the NW one being redder with respect to the main galaxy body. It is interesting to notice that although some of these extraplanar features may be very faint, most of them are present at all wavebands.

SOS 61086 is a disc galaxy seen almost edge-on showing some distortion in the optical images. This is most probably due to an irregular distribution of dust, since in the *K* band the galaxy looks much more symmetrical (see Section 6.3).

SOS 61086 could be affected by the presence of the close companion galaxy SOS 61087. The redshift of this neighbour is  $z = 0.04367$ , implying an LOS velocity of  $+304 \text{ km s}^{-1}$  relative to SOS 61086. While this companion galaxy appears much more compact than SOS 61086, its estimated stellar mass is  $1.3\times$  higher.

The main properties of SOS 61086 and SOS 61087 are listed in Table 1. The Kron magnitudes in the table are corrected for Galactic extinction following Schlafly & Finkbeiner (2011).

From the ultraviolet (UV) and mid-infrared (mid-IR) fluxes, we estimate a global star formation rate  $\text{SFR} = 1.40^{+0.26}_{-0.16} \text{ M}_{\odot} \text{ yr}^{-1}$  (of which 47 per cent is obscured; Haines et al. 2011). For the stellar mass, we adopted the calibration of the GAMA survey (Taylor et al. 2011). For the characterization of the dark-matter haloes, we adopted the models by Di Cintio et al. (2014b), which account for the dependence of the halo properties on the central galaxy (equation 1 of Di Cintio et al. 2014b).

## 2.2 SOS 90630

SOS 90630, at redshift  $z = 0.04817$  ( $V_h = 14093 \text{ km s}^{-1}$ ), is located at  $226 \text{ kpc}$  in projection from the X-ray centre of the cluster SC 1327–312 ( $M_{\text{cl}} \sim 3 \times 10^{14} \text{ M}_{\odot}$ ; Ragone et al. 2006) in the SSCC (see Section 8). The centre of SC 1327–312 is well defined with the peak of X-ray emission coinciding with a bright elliptical galaxy (6dF J1329477–313625,  $z = 0.05017$ ,  $V_h = 14664 \text{ km s}^{-1}$ ). The central velocity of the group is slightly lower at  $14429 \text{ km s}^{-1}$  ( $z = 0.04935$ ) and the velocity dispersion is  $535 \pm 17 \text{ km s}^{-1}$ . This suggests a LOS peculiar velocity of SOS 90630 with respect to the main group of about  $-300 \text{ km s}^{-1}$ .

The *gri* composite VST image in Fig. 4 was derived from images with seeing  $0.6 \text{ arcsec}$  in the *gr* bands and  $0.5 \text{ arcsec}$  in the *i* band. The light distribution of SOS 90630 is highly asymmetric with a prominent western arm in the direction where the disc seems more extended. SF knots and dust obscured regions are found in the centre. Hints of matter flowing out of SOS 90630 towards west are visible in Fig. 5 in all bands.

The main properties of SOS 90630 and SOS 90090 are listed in Table 1. For SOS 90630, we measured a global  $\text{SFR} = 2.50^{+0.72}_{-0.44} \text{ M}_{\odot} \text{ yr}^{-1}$  (of which 74 per cent is obscured; Haines et al. 2011). SOS 90090 has a  $5\times$  lower SFR and  $4.6\times$  higher stellar mass (see Table 1). Using the same parametrizations as for SOS 61086, we estimate the stellar mass and mass halo of SOS 90630 listed in Table 1.

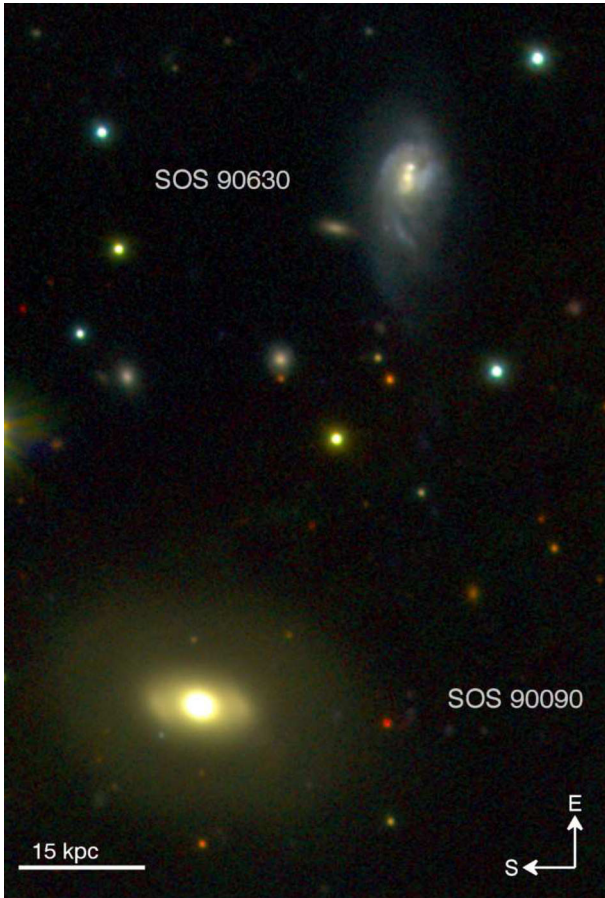
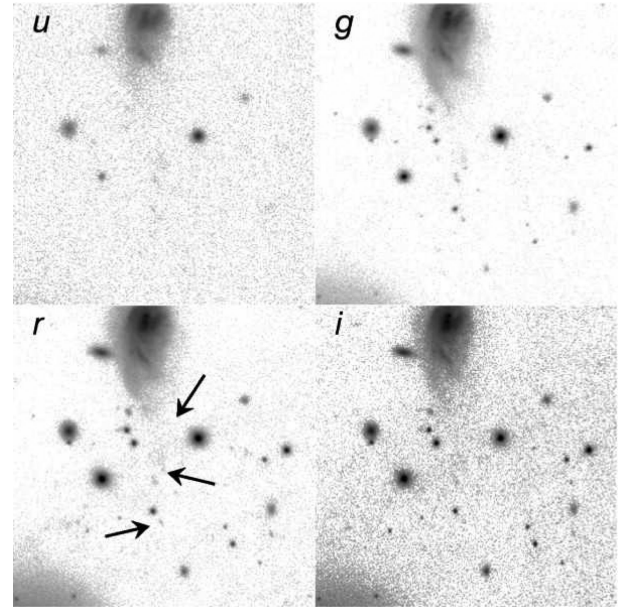
We notice that in the optical (*gri*) images SOS 90630 presents two peaks of brightness in the centre, but this is due to dust absorption as demonstrated in Appendix A and Section 7.

**Table 1.** Properties of SOS 61086 and SOS 90630 and their neighbouring galaxies.

Property	SOS 61086	SOS 61087	SOS 90630	SOS 90090
<i>Coordinates</i>				
ShaSS <sup>1</sup>	13 31 59.80 –31 49 22.2	13 31 59.85 –31 49 04.0	13 29 28.53 –31 39 25.6	13 29 23.43 –31 39 51.7
<i>Magnitudes/fluxes</i>				
$u^a$ , 1	$17.81 \pm 0.03$	$20.06 \pm 0.03$	$17.41 \pm 0.03$	$17.58 \pm 0.03$
$g^a$ , 1	$16.62 \pm 0.03$	$18.36 \pm 0.03$	$16.39 \pm 0.03$	$15.60 \pm 0.03$
$r^a$ , 1	$16.30 \pm 0.03$	$17.44 \pm 0.03$	$16.06 \pm 0.03$	$14.70 \pm 0.03$
$i^a$ , 1	$16.23 \pm 0.03$	$17.23 \pm 0.03$	$15.96 \pm 0.03$	$14.43 \pm 0.03$
24 $\mu\text{m}^2$	$4007 \pm 222 \mu\text{Jy}$		$11013 \pm 573 \mu\text{Jy}$	$3136 \pm 180 \mu\text{Jy}$
1.4 GHz <sup>3</sup>	0.89 mJy		2.30 mJy	
<i>Masses</i>				
Stellar mass <sup>4</sup>	$3.61 \times 10^9 M_\odot$	$4.85 \times 10^9 M_\odot$	$1.0 \times 10^{10} M_\odot$	$8.72 \times 10^{10} M_\odot$
Total halo mass <sup>4</sup>	$1.9 \times 10^{11} M_\odot$	$2.20 \times 10^{11} M_\odot$	$2.5 \times 10^{11} M_\odot$	$5.0 \times 10^{11} M_\odot$
<i>Distances</i>				
Redshift <sup>1</sup>	$0.04261 \pm 0.00023$	$0.04367 \pm 0.00031$	$0.04817 \pm 0.00042$	$0.04929 \pm 0.00022$
Heliocentric velocity <sup>1</sup>	$12502 \pm 69 \text{ km s}^{-1}$	$12806 \pm 93 \text{ km s}^{-1}$	$14093 \text{ km s}^{-1}$	$14413 \pm 66 \text{ km s}^{-1}$
Projected distance <sup>4</sup> to the parent cluster centre	282 kpc		226 kpc	
<i>Star formation rates</i>				
UV+IR global SFR <sup>2</sup>	$1.4 M_\odot \text{ yr}^{-1}$		$2.5 M_\odot \text{ yr}^{-1}$	$0.5 M_\odot \text{ yr}^{-1}$
H $\alpha$ global SFR <sup>4</sup>	$1.76 \pm 0.56 M_\odot \text{ yr}^{-1}$		$3.49 \pm 1.07 M_\odot \text{ yr}^{-1}$	

Notes. <sup>a</sup>Magnitudes in the AB photometric system.

Sources: <sup>1</sup>Merluzzi et al. (2015); <sup>2</sup>Haines et al. (2011); <sup>3</sup>Miller (2005); <sup>4</sup>this work.


**Figure 4.** Composite *gri* image of the field including SOS 90630 (top) and SOS 90090 (bottom).

**Figure 5.** Detail of the field of Fig. 4 shown in the *ugri* bands, with hints of (low-brightness) extraplanar material highlighted by the arrows on the *r*-band image.

### 3 INTEGRAL-FIELD SPECTROSCOPY

The IFS data of SOS 61086 and SOS 90630 were obtained during two observing runs in 2011 April and 2012 April using the WiFeS (Dopita et al. 2007, 2010) mounted at the Nasmyth focus of the Australian National University 2.3 m telescope located at the Siding Spring Observatory, Australia. WiFeS is an image-slicing integral-field spectrograph that records optical spectra over a contiguous  $25 \text{ arcsec} \times 38 \text{ arcsec}$  field of view. This field is divided into 25 1-arcsec-wide long slits (‘slices’) of 38 arcsec length. WiFeS has two independent channels for the blue and the red wavelength

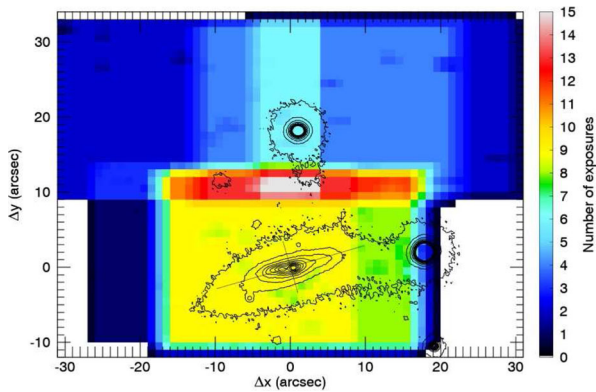




**Figure 6.** *SOS 61086.* WiFeS spatial coverage of the field including *SOS 61086*. The number of exposures covering each part of the field is indicated in the coloured bar. In this figure and in the following maps, the axes indicate the apparent distance from the *K*-band photometric centre in arcsec, the curves are *r*-band isophotes and the two lines crossing the centre mark the apparent major and minor axes and extend to three disc scale radii. With around 6–8 exposures, we reach  $\text{SNR} = 5$  for a flux of  $0.5 \times 10^{-17} \text{ erg s}^{-1} \text{ cm}^{-2} \text{ arcsec}^{-2}$  for the  $\text{H}\alpha$  line.

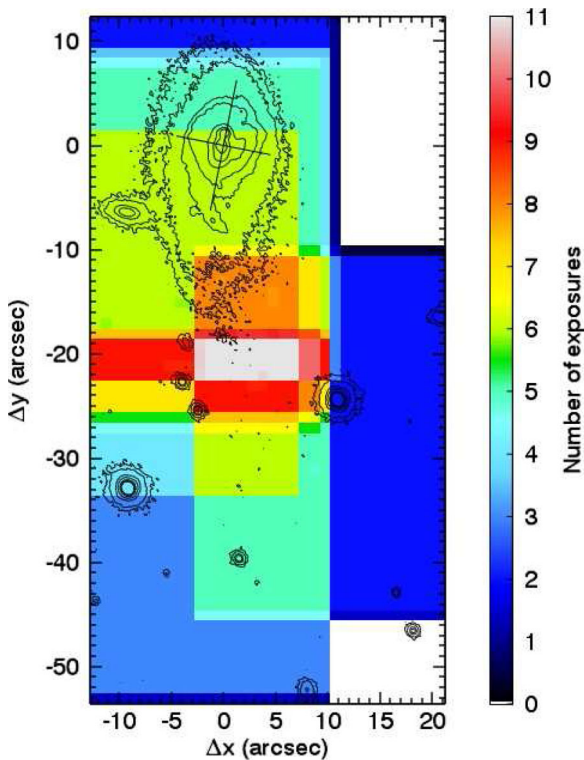


**Figure 7.** *SOS 90630.* Same as Fig. 6 but for *SOS 90630*.

ranges. We used the B3000 and R3000 gratings, allowing simultaneous observations of the spectral range from  $\sim 3300 \text{ \AA}$  to  $\sim 9300 \text{ \AA}$  with an average resolution of  $R = 2900$ . For further details on the WiFeS instrument, see Dopita et al. (2007, 2010).

To cover the galaxies and their surroundings at sufficient depth, we obtained 15 and 11 pointings (45 min each) on *SOS 61086* and *SOS 90630*, respectively. The coverage maps of the two galaxies are shown in Figs 6 and 7. For each exposure on the target, we also acquired the spectrum of a nearby empty sky region with 22.5 min exposure to allow accurate sky subtraction.

We obtained spectra of spectrophotometric standard stars for flux calibration and B-type stars with nearly featureless spectra to determine the telluric correction. Arc and bias frames were also taken for each science exposure. Internal lamp flat-fields and sky flats were taken twice during both runs.

The data were reduced using the WiFeS data reduction pipeline (Dopita et al. 2010) and purposely written FORTRAN and IDL<sup>2</sup> codes (for details see Merluzzi et al. 2013). The WiFeS pipeline performs all the steps from bias subtraction to the production of wavelength- and flux-calibrated data cubes for each of the blue and red channels. The final spectral resolution achieved is  $\sigma \sim 40 \text{ km s}^{-1}$ , and is wavelength and position dependent. The accuracy of the wavelength calibration is  $0.3 \text{ \AA}$ .<sup>3</sup> The data cubes were sampled at  $1 \text{ arcsec} \times 1 \text{ arcsec} \times 1 \text{ \AA}$  and cover a useful wavelength range of  $3800\text{--}8500 \text{ \AA}$ . The data cubes were also corrected for atmospheric differential refraction. Sky subtraction was carried out by means of sky spectra taken closest in time to the galaxy spectra.

The co-addition of individual exposures/pointings was performed taking into account the instrumental spatial distortion as detailed in Merluzzi et al. (2013). The reduced data cubes were corrected for Galactic extinction following Schlegel, Finkbeiner & Davis (1998) and using the extinction curve by Cardelli, Clayton & Mathis (1989) with  $R_V = 3.1$ . The sensitivity of our data is  $0.5 \times 10^{-17} \text{ erg s}^{-1} \text{ cm}^{-2} \text{ arcsec}^{-2}$  at a signal-to-noise ratio  $\text{SNR} = 5$  for the  $\text{H}\alpha$  line, which is usually achieved with 6–8 exposures of 45 min each. Further details on data reduction are given in Merluzzi et al. (2013).

#### 4 $\text{H}\alpha$ IMAGING

$\text{H}\alpha$  imaging of the galaxies *SOS 61086* and *SOS 90630* was obtained with the Maryland-Magellan Tunable Filter (MMTF; Veilleux et al. 2010) on the Magellan-Baade 6.5 m telescope at the Las Campanas Observatory in Chile on 2012 May 21. The MMTF is based on a Fabry–Perot etalon, which provides a very narrow transmission bandpass ( $\sim 5\text{--}12/\text{\AA}$ ) that can be tuned to any wavelength over  $\sim 5000\text{--}9200 \text{ \AA}$  (Veilleux et al. 2010). Coupled with the exquisite image quality provided by active optics on Magellan and the Inamori-Magellan Areal Camera and Spectrograph, this instrument is ideal for detecting extragalactic  $\text{H}\alpha$ -emitting gas. The MMTF 6815–216 order-blocking filter with central wavelength of  $6815 \text{ \AA}$  and full width at half-maximum (FWHM) of  $216 \text{ \AA}$  was used to provide coverage of the  $\text{H}\alpha$  emission line for galaxies belonging to the Shapley supercluster (for details on the instrumental set-up, see Merluzzi et al. 2013).

*SOS 90630* was observed for 75 min in  $\text{H}\alpha$  ( $5 \times 900 \text{ s}$ ) and 30 min in the continuum, by shifting the central wavelength of the etalon  $\sim 60 \text{ \AA}$  bluewards to exclude emission from both the  $\text{H}\alpha$  line and the adjacent  $[\text{N II}]$  lines, and into a wavelength region devoid of major skylines. *SOS 61086* was observed for 45 min in  $\text{H}\alpha$  ( $3 \times 900 \text{ s}$ ) and 15 min in the continuum. The typical image resolution for these exposures was  $0.60 \text{ arcsec}$ .

These data were fully reduced using the MMTF data reduction pipeline,<sup>4</sup> which performs bias subtraction, flat-fielding, skyline removal, cosmic ray removal, astrometric calibration and

<sup>2</sup> <http://www.exelisvis.com/ProductsServices/IDL.aspx>

<sup>3</sup> This is the standard deviation of the difference between the observed wavelength and that predicted by the adopted dispersion relation, averaged over the  $25 \times 38$  spectra of the data cubes.

<sup>4</sup> <http://www.astro.umd.edu/~veilleux/mmtf/dated.html>

stacking of multiple exposures (see Veilleux et al. 2010). Photometric calibration was performed by comparing the narrow-band fluxes from continuum-dominated sources with their known  $R$ -band magnitudes obtained from our existing SOS images. Conditions were photometric throughout, and the error associated with our absolute photometric calibration is  $\sim 10$  per cent. The effective bandpass of the Lorentzian profile of the tunable filter of  $\pi/2 \times \text{FWHM}$  is then used to convert the observed measurements into  $H\alpha$  fluxes in units of  $\text{erg s}^{-1} \text{cm}^{-2}$ . The  $\Delta\lambda$  of the filter is sufficiently narrow that there should be little or no contamination from  $[\text{N II}]$  emission.

The data were obtained in dark time resulting in very low sky background levels, with  $1\sigma$  surface brightness fluctuations within a 1 arcsec diameter aperture of  $0.2 \times 10^{-17} \text{ erg s}^{-1} \text{cm}^{-2} \text{Å}^{-1} \text{arcsec}^{-2}$  implying a sensitivity of  $H\alpha$  imaging of  $1.0 \times 10^{-17} \text{ erg s}^{-1} \text{cm}^{-2} \text{arcsec}^{-2}$  at  $\text{SNR} = 5$ , somewhat less than for the sensitivity of the spectroscopy.

## 5 DATA ANALYSIS

In order to derive a robust estimate of the emission-line fluxes, the contribution of the stellar continuum must be identified and subtracted from the spectrum to leave the pure emission-line spectrum. The stellar continuum modelling, accounting for the dust extinction, also allows us to infer stellar population ages in different galaxy regions. The emission-line fluxes are used to estimate (i) the gas kinematics; (ii) the line-ratio diagnostics; (iii) the dust attenuation and SFR across the galaxy. Details of this analysis are given in Merluzzi et al. (2013); here we briefly summarize the different steps of the procedures.

### 5.1 Stellar continuum modelling and subtraction

Late-type galaxies present complex SF histories with continuous bursts of SF from the earliest epochs right up until the present day (Kennicutt 1983; Kennicutt, Tamblyn & Congdon 1994; James, Prescott & Baldry 2008; Williams et al. 2011). We thus attempt to fit the stellar continuum of our target spiral galaxies as a linear combination of 40 simple stellar populations (SSPs) from the Vazdekis et al. (2010) stellar population models covering the full range of stellar ages (0.06–15 Gyr) and three different metallicities  $[\text{M}/\text{H}] = -0.41, 0.0, +0.22$ . The models assume a Kroupa (2001) initial mass function (IMF). They are based on the Medium resolution INT Library of Empirical Spectra of Sánchez-Blázquez et al. (2006), have a nominal resolution of 2.3 Å, close to our instrumental resolution, and cover the spectral range 3540–7410 Å.

The spectra were smoothed spatially (using a  $3 \times 3$  spaxel region within the main galaxy body) to achieve an  $\text{SNR}$  of  $\sim 40/\text{Å}$  for the stellar continuum at  $\sim 4600\text{--}4800$  Å. For each spaxel, the spatially smoothed spectrum from the blue arm was fitted with the Vazdekis et al. (2010) models after masking out regions below 3950 Å, which have significantly reduced S/N levels and flux calibration reliability, above 5550 Å, where a bright sky line is located, and regions affected by emission lines. The spectral pixels masked are kept fixed for all spaxels, and for each emission line we carefully examine each data cube to identify the full range of spectral pixels that are affected by the emission/sky line for at least one spaxel, ensuring that the mask is sufficiently generous to account for the shift of the emission line due to velocity gradients across the galaxy (including the extragalactic gas). After continuum subtraction, we check the data cube representing the residual emission-line spectrum to confirm that all apparent emission lines (including very faint ones) have been completely covered by the masks. The best-fitting linear

combination of SSPs to the spatially smoothed spectrum is then renormalized to fit the spectrum from the individual spaxel (again excluding the masked spectral pixels). This process allows us to subtract the continuum for spaxels in the outer regions of the galaxy where there is a clear detection of the continuum, but the  $\text{SNR}$  is much too low to reliably fit complex stellar population models.

This best-fitting model was then extended to the red arm, and varying only the global scaling factor to account for any (slight) mismatch in the flux calibrations between red and blue arms, and subtracted from the red arm spectrum, to produce the pure emission spectrum for the corresponding spaxel in the red arm. Details on the stellar continuum modelling are given in Merluzzi et al. (2013).

In Figs 8 and 9, we show two example outputs of our stellar continuum fitting process. The input spectrum (black curve) is from a  $3 \times 3$  spaxel region in the centre of the galaxy. The resultant best-fitting stellar continuum (magenta curve) comprising a linear combination of SSPs requires both young and old (thin blue/red curves) components. The shaded regions correspond to wavelength ranges not considered in the fitting process, including the masks for emission lines. This stellar continuum is subtracted from the observed spectrum to produce the residual emission component (thick blue curve) accounting now for stellar absorption, revealing clear emission at  $\text{O II}$ ,  $\text{H}\zeta$ ,  $\text{H}\epsilon$ ,  $\text{H}\delta$ ,  $\text{H}\gamma$ ,  $\text{H}\beta$  and  $[\text{O III}]$ . The Balmer emission lines are all located within deep absorption features, demonstrating the necessity of accurately modelling and subtracting the stellar continuum prior to measuring these lines. Outside of the emission lines, the rms levels in the residual signal are consistent with expectations from photon noise, with little remaining structure. This holds true throughout the galaxy indicating that on a spaxel-by-spaxel basis the model fits to the stellar continuum are formally good ( $\chi^2_{\nu} \sim 1$ ).

The inverse problem of recovering the SF history of galaxies from their spectra is potentially ill-posed, and small perturbations of the data due to noise can introduce large perturbations in the best-fitting stellar age distribution, at least in terms of the relative contributions from individual SSPs. To modulate this, many stellar population fitting codes employ a regularizing method to minimize the curvature (burstiness) of the SF history while still being consistent with the observations. As our primary objective is to accurately model the spectrum and subtract the continuum so that it does not bias our emission-line analyses, and map the stellar kinematics, our code does not include a regularization step or require the solution to be a relatively smooth function of age. We confirm that the addition of random noise (at the levels of the sky background) can significantly affect the relative contributions from individual SSPs, but that this is mostly just shifting weights among the SSPs that are adjacent in terms of stellar age (they are separated by just 0.1 dex). When consolidating the contributions into a small number of age ranges, such as above and below 1 Gyr, the perturbations due to noise on the best-fitting model SF history are much less dramatic, barely shifting the relative normalizations of the thin red and blue curves in Fig. 8. We caution the reader to consider our descriptions of the SF history obtained from this continuum fitting to be qualitative rather than finely structured.

### 5.2 Emission-line measurements

Emission-line fluxes and widths were measured with Gaussian fitting. Where lines are either partially overlapping or close (as in the cases of  $[\text{N II}]-\text{H}\alpha$ - $[\text{N II}]$ ,  $[\text{S II}]$  6717–6731 and  $[\text{O III}]$  4959–5007), the lines were fitted simultaneously but independently to test our results against those line pairs having fixed flux ratios. The

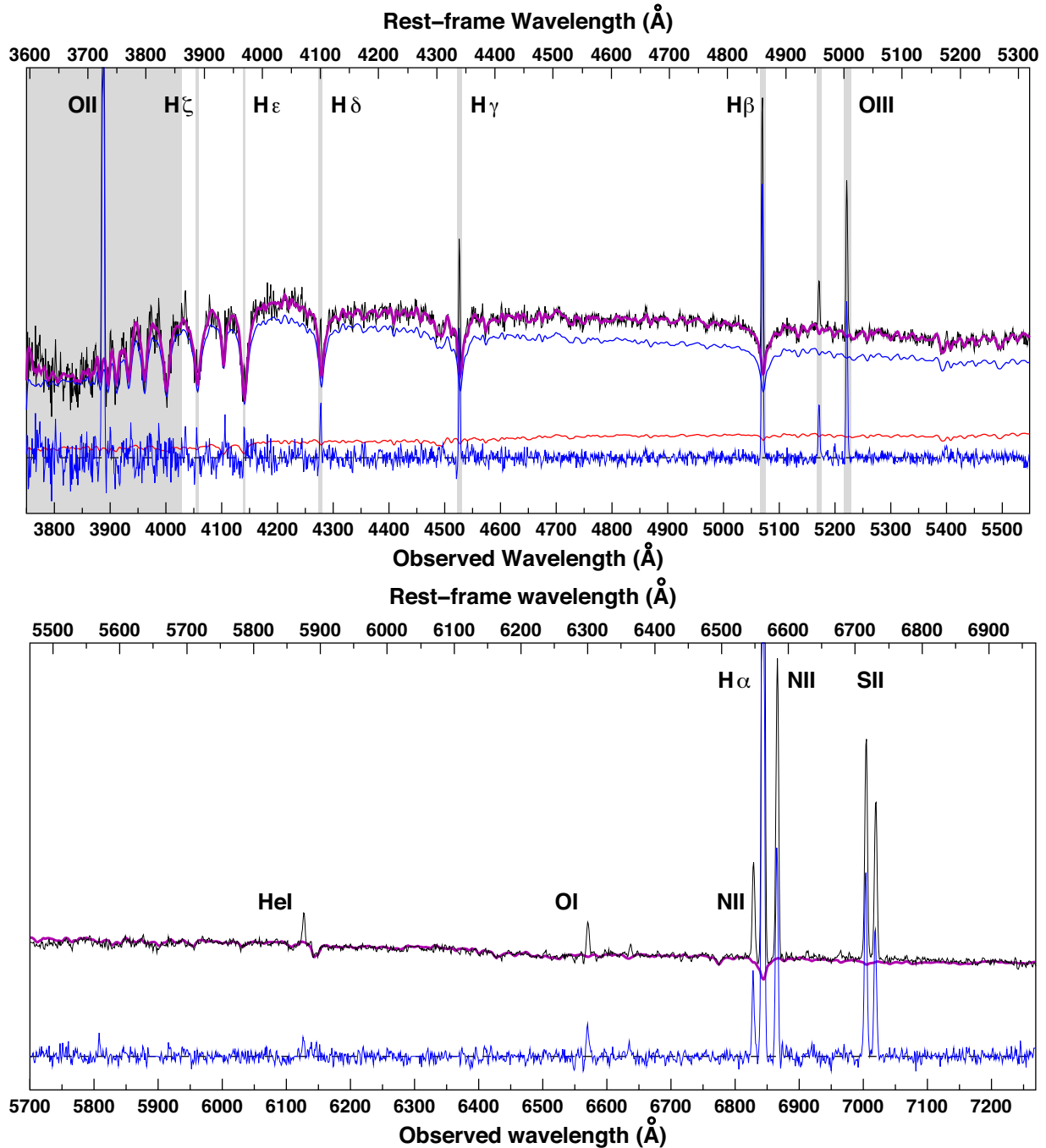


**Figure 8.** *SOS 61086*. Example results from the stellar continuum fitting process of the blue arm of *SOS 61086* (upper panel) and extrapolated to the red arm (lower panel). In the upper panel, the black curve shows the input spectrum, coming from the  $3 \times 3$  spaxel region around the photometric centre of the galaxy. The magenta curve shows the resultant best-fitting stellar continuum comprising a linear combination of SSPs, requiring both old ( $>1$  Gyr; thin red curve) and young ( $<1$  Gyr old; thin blue curve) components. The shaded regions indicate the wavelength ranges excluded from the fitting process, including the masks for emission lines. The residual emission component (thick blue curve) reveals clear emission at [O II]  $\lambda 3729$ , H $\zeta$ , H $\epsilon$ , H $\delta$ , H $\gamma$ , H $\beta$  and [O III]  $\lambda\lambda 4959, 5007$  in the blue arm (upper panel) and the emission lines of [O I], H $\alpha$ , [N II], [S II].

uncertainties in the derived quantities were evaluated through numerical simulations.

At  $\text{SNR} = 5$ , the relative errors from the fit for both flux and  $\sigma$  are  $\sim 30$  per cent. The total error on the flux also accounts for the uncertainty in the flux zero-point, which amounts to  $\sim 8$  per cent.

The main contribution to the uncertainty on the radial velocity comes from the uncertainty in the wavelength calibration

( $\sim 13 \text{ km s}^{-1}$ ), while the error from the fit is very small ( $< 5 \text{ km s}^{-1}$ ). We assume a conservative uncertainty of  $\Delta V \sim 15 \text{ km s}^{-1}$ . The total error on the velocity dispersion accounts for the error from the fit ( $\sim 1\text{--}10 \text{ km s}^{-1}$ ) and the uncertainty of  $\sim 5 \text{ km s}^{-1}$  on the value of the instrumental width.

In Merluzzi et al. (2013), we have shown that, in order to obtain flux ratios with uncertainties lower than 30 per cent, the



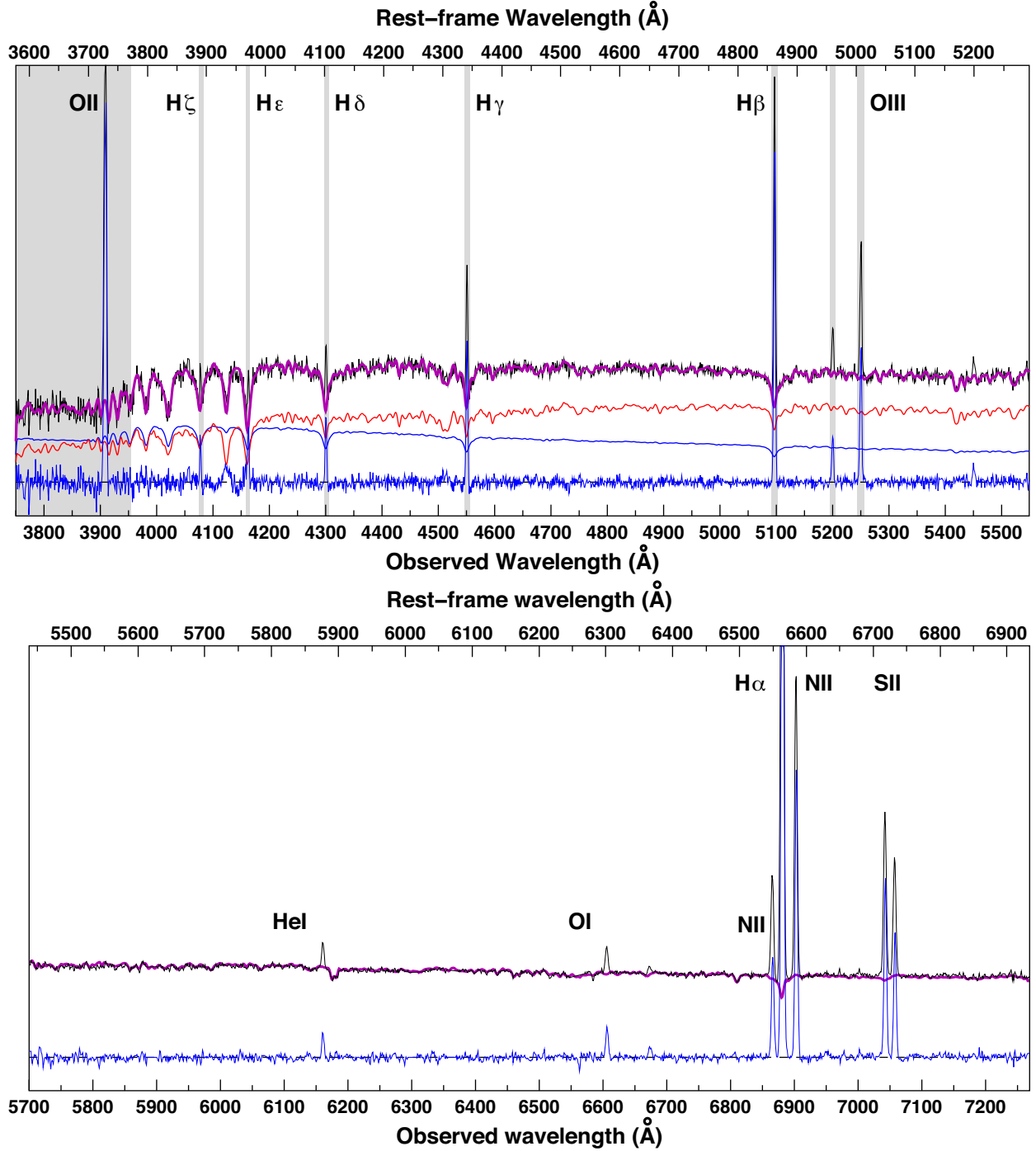
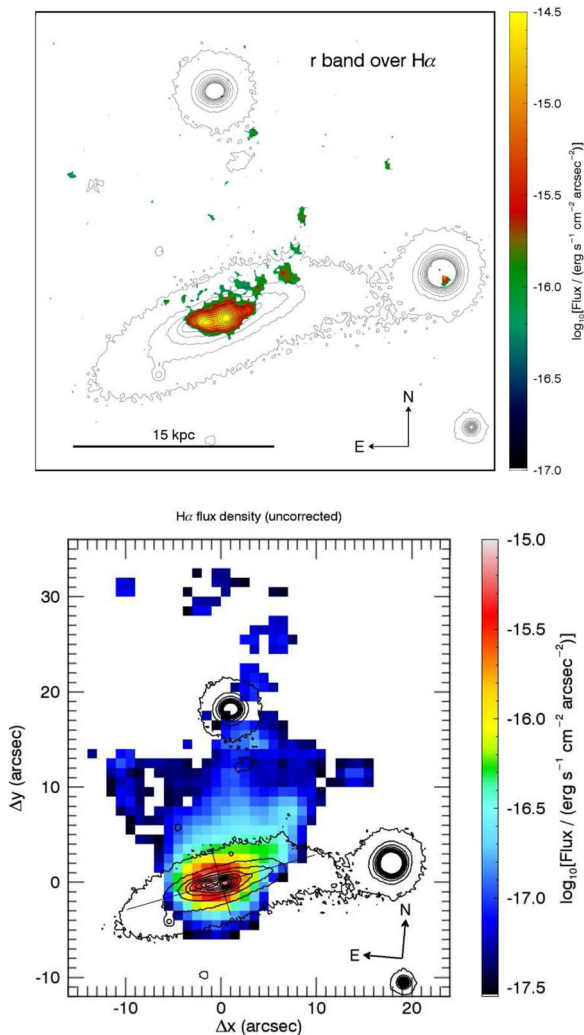


Figure 9. *SOS 90630*. Same as in Fig. 8, but for *SOS 90630*.

individual lines must have  $\text{SNR} > 20$ . To achieve these SNRs, we spatially binned the data by means of the ‘*weighted Voronoi tessellation*’ (WVT) method by Diehl & Statler<sup>5</sup> (2006) which attempts to reach a target SNR in all bins. The WVT performs a partitioning of a region based on a set of points called ‘generators’, around which the partition of the plane takes place. The partitioning is repeated iteratively until a target SNR is achieved in all bins. The advantage of the WVT with respect to the Voronoi tessellation is

the possibility to ‘manually’ choose a number of generators on the basis of their position within the galaxy. The faintest line involved in our flux ratios is the  $[\text{O I}] \lambda 6300$  line, which is  $\sim 5 \times$  fainter than  $\text{H}\alpha$ , so that we set to 100 the target SNR of  $\text{H}\alpha$ . For spatial consistency, we manually adjusted some of the WVT regions. The 35 and 48 galaxy regions identified by the WVT for *SOS 61086* and *SOS 90630* respectively are shown in Figs 13 and 21 (see Sections 6.3 and 7.3, respectively). The spatial binning of the data was applied for the derivation of flux ratios, dust attenuation and SFR, but not for the kinematics, for which no binning was necessary.

<sup>5</sup> <http://www.phy.ohiou.edu/diehl/WVT>



**Figure 10.** *SOS 61086*. Top: contours of the *r* band over the MMTF  $H\alpha$  image. Bottom:  $H\alpha$  flux derived from IFS data. The *r*-band contours are shown in red and the  $H\alpha$  flux in black. Here and in the following figures, the scales give the distance (in arcsec) from the photometric centre of the galaxy. The major and minor axis are marked by lines of length three times the disc scale radius.

## 6 SOS 61086: RESULTS

### 6.1 Morphology of the $H\alpha$ emission

The narrow-band  $H\alpha$  image and the distribution of  $H\alpha$  emission derived with WiFeS are shown in Fig. 10 (upper and lower panel, respectively). Since the  $H\alpha$  imaging is both sharper and shallower than the WiFeS data, the two data sets are complementary and together show different aspects of the distribution of ionized gas. The IFS data show that ionized gas spreads out from the disc of the galaxy in an approximately triangular region with a vertex in the central disc and one side at  $\sim 16$  kpc north and directed approximately E-W. No ionized gas is found in the disc beyond  $\sim 6$  kpc from the centre along the major axis. Along the minor axis, instead, the ionized gas appears to extend far out from the disc in projection. Other clumps of gas extend further in the north reaching  $\sim 30$  kpc in projection. The  $H\alpha$  flux is maximum in the centre and is directed along a main stream in the NW direction. Three secondary maxima of flux are found along the northern side. The narrow-band image resolves the nuclear emission in two main clumps lying around the

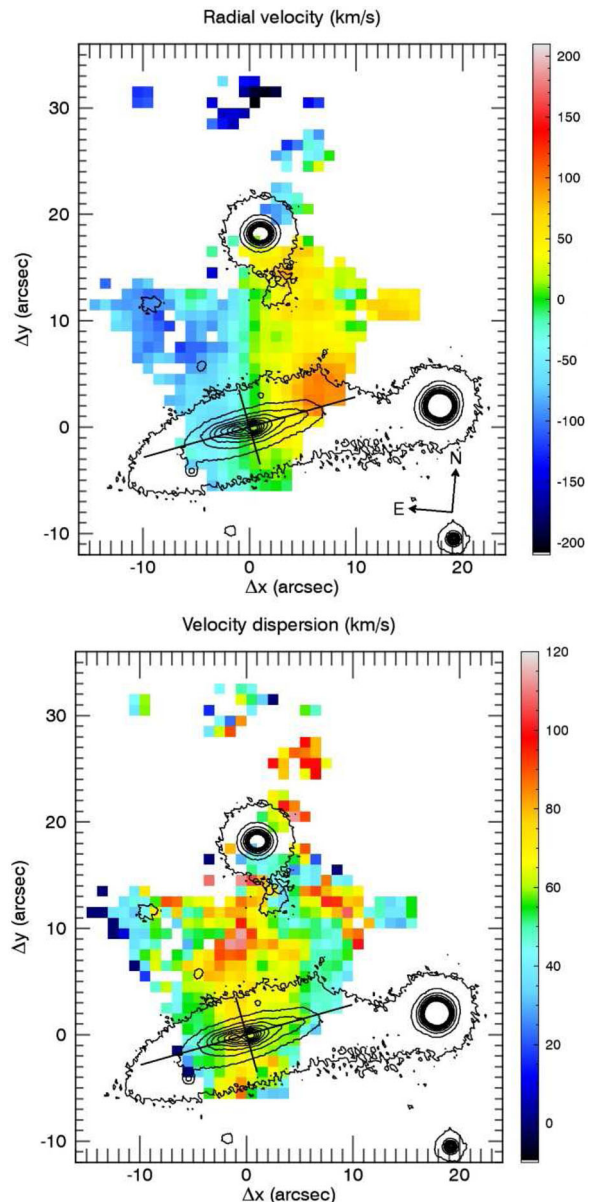


**Figure 11.** *SOS 61086*. Gas kinematics derived from the fit to the  $H\alpha$  emission line. The black contours mark the surface brightness distribution of the *r*-band image, while the black lines, extending  $3\times$  the disc scale radius, show the positions of the minor and major axis and cross at the *K*-band photometric centre. Top: gas velocity field. Each pixel is colour coded according to the measured radial velocity relative to the galaxy centre. Bottom: gas velocity dispersion. The velocity scales are on the right of each panel.

photometric centre as determined by the maximum in *K*-band flux. The NW stream is also resolved in a chain of major emission clumps departing from the centre. Other  $H\alpha$  clumps are also detected in N and NE directions. The nearby galaxy *SOS 61087* does not show any  $H\alpha$  emission associated with it.

### 6.2 Gas and stellar kinematics

The radial velocity field of the gas derived from  $H\alpha$  is shown in the top panel of Fig. 11. The black contours trace the *r*-band stellar continuum derived from VST imaging. The black lines mark the major and minor axes of the disc extending to  $3\times$  the

disc scale radius, and crossing at the  $K$ -band photometric centre. The kinematic centre coincides with the photometric centre of the  $K$ -band image.

Given the strong perturbation experienced by the gas, the most remarkable feature of this velocity field is the large-scale regular motion. Overall, the gas appears to rotate around an axis extending  $\sim 12$  kpc (in projection) north from the galaxy centre, well beyond the stellar disc. This ‘rotation axis’ bends westwards south from the centre. Superimposed to the large-scale motion, there are however some significant local maxima and minima in radial velocity, like for instance an area at  $\sim 7$  kpc W from the centre and  $\sim 1$  kpc N from the disc, with  $V \sim 85$  km s $^{-1}$ . The distant shreds of gas in the north do not seem to participate in this overall motion, being generally blueshifted with respect to the average.

The gas velocity dispersion  $\sigma$  (Fig. 11, bottom panel) is generally higher than expected for normal turbulent H II regions ( $\sigma \sim 20$ – $30$  km s $^{-1}$ ). As expected,  $\sigma$  is higher where the radial velocity gradients are larger. But in some areas it reaches values as high as  $100$  km s $^{-1}$ , such as in the region about  $8$  kpc N from the centre. Such high values most probably witness the presence of complex motions of different gas elements along the LOS.

From the fit of the stellar continuum, we derived the velocity field of the stars shown in Fig. 12. The stellar velocity field is fairly symmetric in the inner  $\sim 4$  kpc. The kinematic axis is skewed with respect to the minor axis, reflecting the presence of non-circular motions, most probably to the presence of a bar. This axis is aligned with the kinematic axis of the gas. Also the shape of the velocity field bears some resemblance with the gas, but the comparison of the two velocity profiles (lower panel of Fig. 12) shows that the two components are clearly decoupled. The shape of the minor-axis velocity profile of the stars is consistent with the non-circular motions due to a bar.

As a note of caution, we must remark that the presence of dust adds complications to the interpretation of the kinematics, since dust may selectively hide parts of the moving gas or stars (e.g. Giovanelli & Haynes 2002; Baes et al. 2003; Kregel, van der Kruit & Freeman 2004; Valotto & Giovanelli 2004).

### 6.3 Dust extinction across the galaxy

For the subsequent analysis of this galaxy, we binned the spatial pixels to achieve the needed SNR as explained in Section 5.2. Only the pixels with  $\text{SNR}(\text{H}\alpha) > 8$  were considered to make the bins.<sup>6</sup> The 35 regions so identified are shown in Fig. 13.

The distribution of the dust attenuation derived for each of these regions from the  $\text{H}\alpha/\text{H}\beta$  line ratio, given in terms of the  $V$ -band extinction  $A_V$ , is shown in the upper panel of Fig. 14. Here we adopted an intrinsic ratio of 2.87 (the ‘case B’ recombination). In doing so, we implicitly assume that the extraplanar gas is in the conditions of typical H II regions, in which the primary source of ionization is ongoing SF. Other sources of ionization such as thermal conduction, shock heating or magnetohydrodynamic processes (e.g. Veilleux et al. 1999; Boselli et al. 2016) might be at work in the tail, in which case the actual  $A_V$  would be significantly different from the one estimated here. This is certainly the case for the NE region of the tail (light grey in Fig. 15), which we show below to be dominated

<sup>6</sup> In spaxels with  $\text{SNR}(\text{H}\alpha) \sim 3$ , many fainter lines (notably  $[\text{O I}]\lambda 6300$ ) are not even visible. We therefore adopted a higher threshold for  $\text{SNR}(\text{H}\alpha)$ , with a value around 8 representing a good compromise between quality and extension of the measured area.

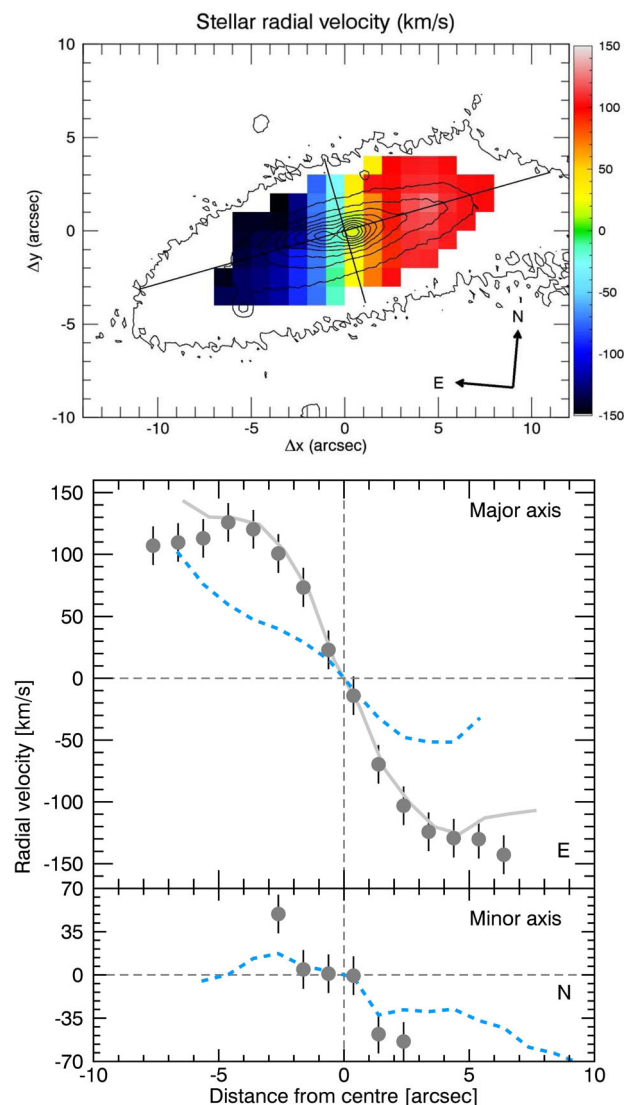


**Figure 12.** *SOS 61086*. The stellar velocity field (top). Same symbols and  $r$ -band contours as in Fig. 11. Radial velocity profiles along the major and minor axis (bottom) of stars (grey dots) and gas (blue dashed curve). The grey curve is the flipped stellar velocity profile, plotted to assess its symmetry. Errors of  $15$  km s $^{-1}$ , mainly coming from wavelength calibration, are indicated.

by shock heating. For the rest of the tail, the continuum emission detected in the whole UV–optical wavelength range ( $u$  to  $i$ ), the presence of compact emission regions witnessed by the  $\text{H}\alpha$  image and the diagnostic diagrams (see below) make us confident that most of the detected emission is associated with SF (e.g. Yoshida et al. 2012). We adopted the theoretical attenuation curve by Fischera & Dopita (2005) with  $R_V = 4.5$ . The highest dust extinction ( $A_V \sim 2.5$ – $2.9$  mag) is observed in two regions covering the NW disc and the extraplanar gas just out of the disc. The asymmetric distribution of the dust extinction strengthens our hypothesis on the apparent bending of the disc (Section 2.1). Moderate ( $A_V \sim 1.5$  mag) dust attenuation is observed in the galaxy centre, while the southern part of the disc and the NW tail of the extraplanar gas suggest a lower dust content.



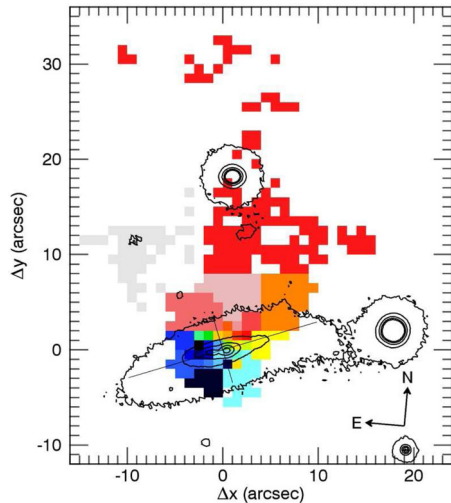


**Figure 13.** *SOS 61086*. The 35 galaxy regions identified by the WVT are shown in different colours. For each of these regions, reliable and robust measurements of emission-line ratios are derived. The colour coding shown here is used to identify the region corresponding to each symbol in Fig. 15.

#### 6.4 Ongoing SF and recent SF history

We derive the current SFR from the  $H\alpha$  flux taking into account the effects of dust extinction following Kennicutt (1998) and adopting the Kroupa IMF. The SFR surface density across the galaxy is given in the bottom panel of Fig. 14. The integrated  $H\alpha$ -derived SFR of *SOS 61086* amounts to  $1.76 \pm 0.56 M_{\odot} \text{ yr}^{-1}$  where the error takes into account the uncertainties related to the flux and attenuation measurements added to a 30 per cent uncertainty due to the different calibrations of  $H\alpha$  as an SFR indicator (Kennicutt 1998). The contribution to the SFR from the NE (shock-dominated, see Section 6.5) tail is not considered. Half of the SF occurs in a central region of 2.5 kpc radius. Lower SFR is detected in the external disc and the extraplanar gas close to the disc. The SFR value in the gas tail far from the disc suggests that SF is low in the detached gas. The integrated  $H\alpha$ -derived SFR is consistent with that derived from UV and IR data (see Table 1).

The recent SF history across the disc is constrained by the stellar continuum modelling described in Section 5.1. In the centre of *SOS 61086*, where the density of SF appears highest (see Fig. 8, upper panel), the emission from the stellar continuum appears relatively blue, peaking at  $\sim 4000 \text{ \AA}$  (rest-frame). This reflects the dominant young stellar population in the centre of the galaxy, with stars younger than 1 Gyr (thin blue curve in Fig. 8, upper panel) contributing 85 per cent of the luminosity at  $4000 \text{ \AA}$ , and 24 per cent of the stellar mass. This dominance of young stars is supported by the deep  $H\delta$  and  $\text{Ca II H}$  absorption features, which give rise to low values of the  $\text{Ca II H}$  index (0.65, defined as the ratio of the counts in the bottom of the  $\text{Ca II H+H}\epsilon$  and  $\text{Ca II K}$  lines; Rose 1985) and the  $H\delta/\text{Fe I } \lambda 4045$  index (0.53), indicative of an ongoing/recently terminated starburst that dominates the integrated light at  $4000 \text{ \AA}$  (Leonardi & Rose 1996). Our stellar modelling of the young component suggests a continuous steady SFR over the full range 60–1000 Myr, with 16 per cent of the stellar mass within this young component coming from stars younger than 200 Myr. This sustained  $\sim 2 \times$  increase in SF is still ongoing as implied by the strong  $H\alpha$  emission in this region with  $\text{EW}(H\alpha) \sim 60 \text{ \AA}$  (see Fig. 8, lower panel). Further Balmer emission lines are visible in Fig. 8, from  $H\beta$  all the way up to  $H\zeta$  ( $3889 \text{ \AA}$ ).

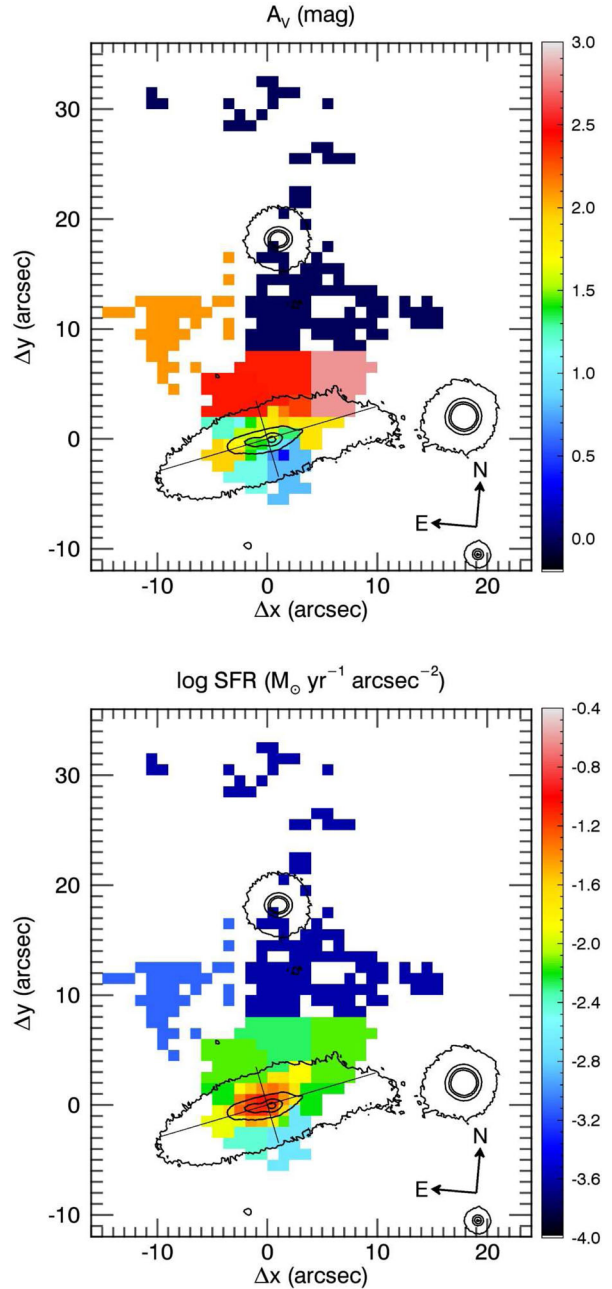


**Figure 14.** *SOS 61086*. Dust attenuation derived from the  $H\alpha/H\beta$  line ratio (top) and attenuation-corrected SFR (bottom). The contribution to the SFR from the NE (shock-dominated) tail is not considered in the analysis.

The old stellar component (red curve) includes both intermediate-age (2–3 Gyr old) and primordial (8–15 Gyr old) components, indicative of a continual formation of stars through the lifetime of the galaxy.

As we move from the centre of the galaxy to the eastern edge, the spectra progressively change from ongoing starburst to post-starburst signatures, with  $\text{EW}(H\alpha)$  declining steadily to zero, and the  $H\delta$  and  $\text{Ca II H}$  absorption lines becoming ever deeper. Here the  $\text{Ca II H}$  index (Rose 1985) falls to a value of just 0.27, while the  $H\delta/\text{Fe I } \lambda 4045$  index also drops to 0.42. Such extreme values are too low for any of the burst models of Leonardi & Rose (1996), but certainly require the entire integrated light at  $4000 \text{ \AA}$  to be due to a recent/ongoing burst. Indeed, our best-fitting stellar population

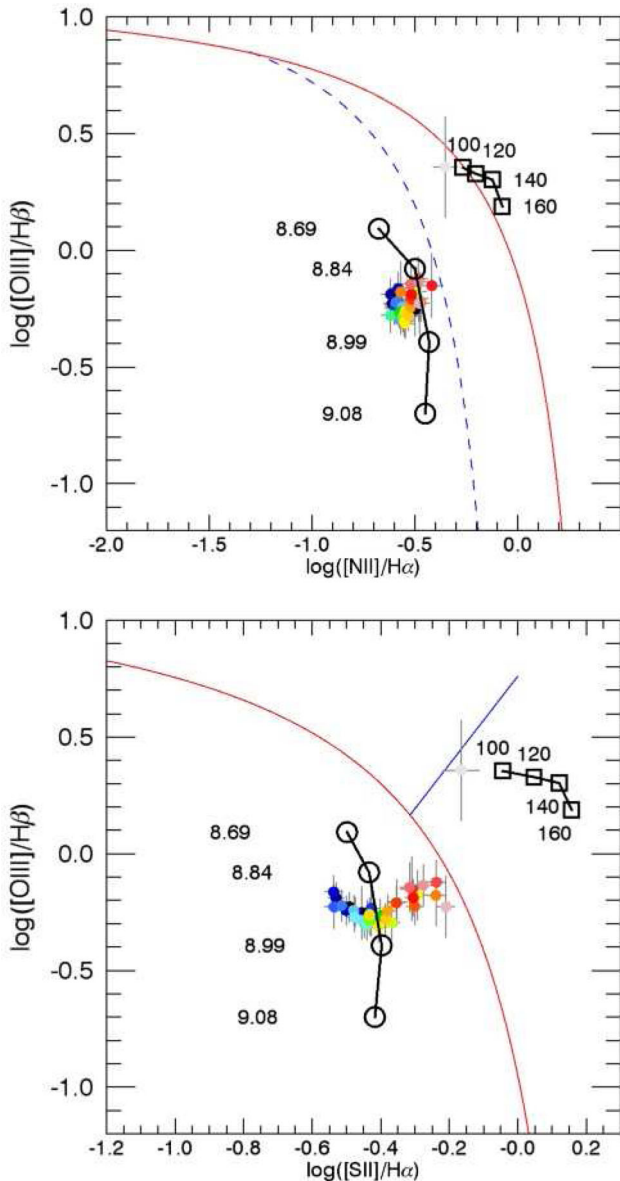


**Figure 15.** *SOS 61086*. Line flux diagnostic diagrams of the different galaxy regions (see the text) colour coded as in Fig. 13. The theoretical (red curve) and empirical (blue dashed curve in the upper panel) upper limits for H II regions are indicated as well as the separation between AGN and LINER (solid blue line in the lower panel). We also show a set of H II region models for fixed ionization parameter  $\log q = 7.0$  and four abundances (open circles), as indicated, along with four shock models with shock velocities in the range  $100\text{--}160\text{ km s}^{-1}$  (open squares).

model has little (if any) contribution from old ( $>1$  Gyr) stellar populations (red curve) in terms of emission, being dominated by  $0.3\text{--}1.2$  Gyr stellar populations with spectra dominated by A-type stars.

### 6.5 Excitation and metallicity of the gas

The line ratios and velocity dispersions observed in the ionized gas enable us to distinguish between gas which is photoionized by H II regions and gas which is excited by shocks. In order to interpret the line-ratio diagnostics, we have run some representative shock and

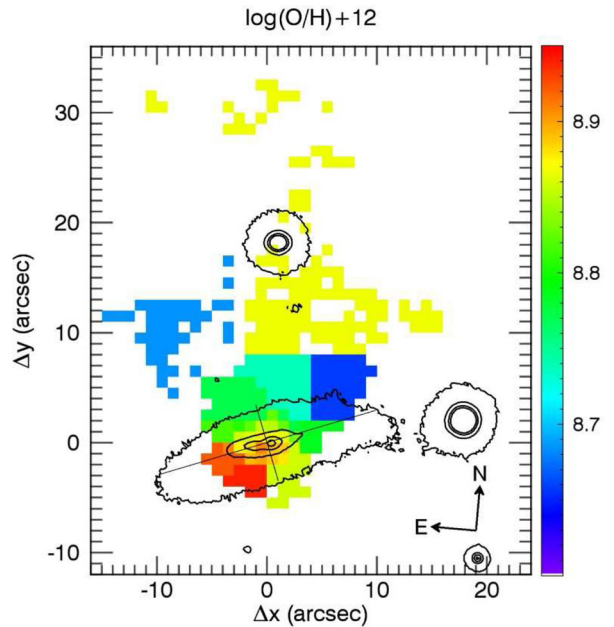


**Figure 16.** *SOS 61086*. Abundance distribution in the galaxy as derived using the PYQZ module.

photoionization models using the modelling code MAPPINGS 4 described in Dopita et al. (2013). In Fig. 15, we show the observations of *SOS 61086* on the standard BPT diagrams (Baldwin, Phillips & Terlevich 1981) as refined by Veilleux & Osterbrock (1987), Kewley et al. (2001, 2006) and Kauffmann et al. (2003). We also plot four H II region models generated as described in Dopita et al. (2013) with an ionization parameter  $\log q = 7.0$  (see below), and four different metallicities (open circles in Fig. 15). We also show, for comparison, four shock models with  $2\times$  solar metallicity ( $12 + \log O/H \sim 8.99$ ) and four different velocities (open squares in Fig. 15). These shock models have fully self-consistent ionization.

In our first study (Merluzzi et al. 2013) and in other cases of RPS galaxies (e.g. Fossati et al. 2016), clear evidence has been found that both photo- and shock-ionization were at work. In *SOS 61086*, the situation with regard to shocks is different. The line ratios cluster over a very narrow range (see Fig. 15) consistent (according to our photoionization models) with gas of somewhat higher than solar metallicity ( $12 + \log O/H \sim 8.8$ ) being ionized mainly by hot stars, except for the NE tail. By comparison of the observations with the shock sequence, it is clear that shocks are important in determining the excitation only in the NE region of the tail.

The tight grouping of points indicates very little sign of an abundance gradient in this galaxy, or in the extraplanar gas associated with it. We have used the PYTHON module PYQZ<sup>7</sup> described in Dopita et al. (2013) to estimate the ionization parameter and the oxygen abundance in each of the 35 galaxy regions identified by the WVT. The ionization parameter spans a narrow ( $\sigma_{\log q} = 0.08$ ) range of values around  $\log q = 6.95$ . The oxygen abundance is shown in Fig. 16 where a rather uniform distribution is seen.

<sup>7</sup> The lines in the PYQZ code are H $\beta$ , [O III]  $\lambda 5007$ , [O I]  $\lambda 6300$ , H $\alpha$ , [N II]  $\lambda 6583$ , [S II]  $\lambda\lambda 6717\text{--}6731$ .

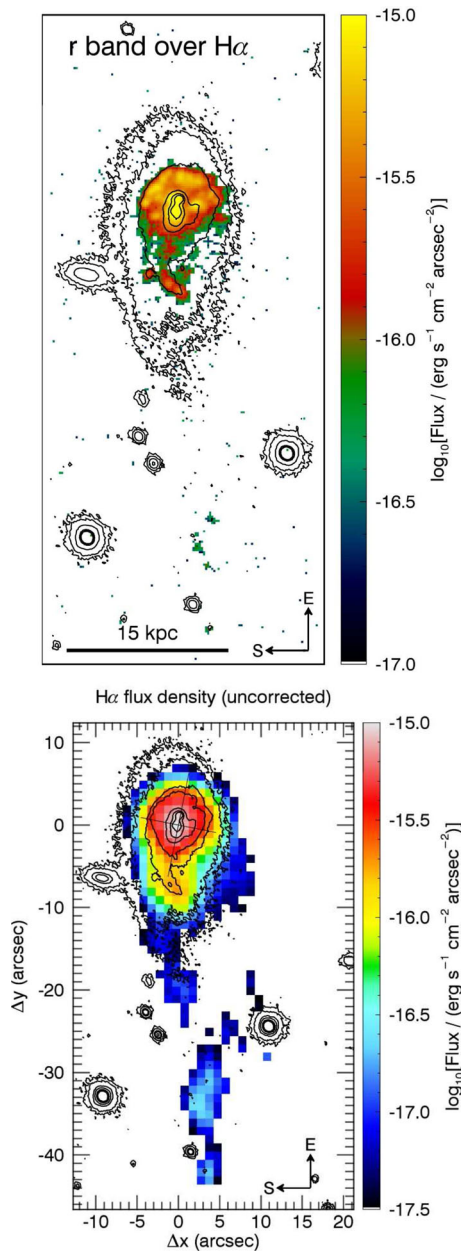


**Figure 17.** *SOS 90630*. Top: contours of the  $r$  band over the MMTF  $H\alpha$  image. Bottom:  $H\alpha$  flux derived from IFS data. The  $r$ -band contours are shown in red and the  $H\alpha$  flux in black.

## 7 SOS 90630: RESULTS

### 7.1 Morphology of the $H\alpha$ emission

The  $H\alpha$  image and the distribution of  $H\alpha$  emission from IFS for *SOS 90630* are shown in Fig. 17 (upper and lower panels, respectively). The ionized gas disc appears truncated in the ESE side. Gas extending  $\sim 4$  kpc in projection out of the disc is seen in the NW side, and more prominently along a tail extending by more than 41 kpc to the west. The maximum of  $H\alpha$  emission takes place in the centre of the galaxy, and is resolved into two clumps about 1 kpc apart in the narrow-band image. The MMTF image resolves an arc-shaped crown composed of  $H\alpha$ -emitting knots all along the leading edge of the galaxy. Other knots of  $H\alpha$  flux are detected along a western arm

and in the tail. The MMTF imaging also reveals compact ( $< 0.5$  kpc)  $H\alpha$  emission at the centre of *SOS 90090*, indicating the presence of an AGN or ongoing nuclear SF activity. The overall morphology of the  $H\alpha$  emission is a remarkable example of the classic ‘jellyfish’ forms reproduced in simulations of galaxies undergoing RPS (e.g. Kapferer et al. 2009).

### 7.2 Gas and stellar kinematics

The velocity fields of the gas in *SOS 90630* are shown in Fig. 18, while Fig. 19 shows the profiles of the gas radial velocity along the major and minor axes in the disc of the galaxy. The kinematic axis (traced by the green colour) is distorted into a U-shape with a concavity directed to the west and is not symmetric with respect to the major axis.

The kinematics of the external gas is continuous with that of the disc. The velocity in the tail smoothly rises from  $\sim -145$  km s $^{-1}$  in the disc to  $\sim -20$  km s $^{-1}$  at the extreme west edge (41 kpc from the centre). Within 5 kpc, where the gas is present on both sides of the disc, the radial velocity is symmetric with respect to the centre (Fig. 19, upper panel). Only in the last kpc in the western disc, we notice an inversion of the trend. The minor-axis profile just reflects the U-shaped kinematic axis.

The velocity dispersion of the gas is fairly uniform in the disc, around  $\sim 60$ – $80$  km s $^{-1}$ , higher ( $\sim 80$ – $120$  km s $^{-1}$ ) in the first part of the tail (17–21 kpc from the centre) and lower (around 50 km s $^{-1}$ ) in the rest of the tail. In the disc, we notice that the region with higher values of  $\sigma$  is also U-shaped like the radial velocity field.

The stellar radial velocity field and profiles, shown in Fig. 20, are almost fully consistent with those of the gas along the major axis, but in the southern part of the minor axis the gas recedes with a velocity higher (by  $\sim 20$  km s $^{-1}$ ) than the stars, indicating that the two components are decoupled outside of the very central ( $\lesssim 2$  kpc) region of the galaxy.

### 7.3 Dust extinction across the galaxy

Similarly to the analysis of *SOS 61086*, we performed a spatial binning of the IFS data to reach the SNR needed for reliable line-ratio measurements. As before, only the pixels with  $\text{SNR}(H\alpha) > 8$  were considered in the analysis. The 48 regions so obtained are shown in Fig. 21. Similarly to *SOS 61086*, the continuum emission (from the  $u$  to  $i$  bands), the presence of compact  $H\alpha$  emission regions and the diagnostic diagrams suggest that the detected emission is mainly associated with SF. In Fig. 22 (upper panel), we show the spatial distribution of the dust attenuation. This has the maximum (at  $\sim 2.4$  mag) in the centre and is enhanced in the NW sector of the disc ( $\sim 1.5$  mag), while decreases in the SE sector ( $\sim 0.9$ – $1.2$  mag). The attenuation in the gas tail ( $\sim 0.9$  mag) indicates a small dust content. The inset of Fig. 22 (upper panel) is a zoom in the centre of the galaxy to show that the western side is more attenuated (by  $\sim 0.8$  mag) than the eastern side in support of the fact that the optical appearance of a double nucleus is an artefact from dust absorption (see Appendix A).

### 7.4 Ongoing SF and recent SF history

The map of SFR in Fig. 22 (lower panel) shows that the highest SF takes place close to the galaxy centre extending across the eastern clumps of  $H II$  regions and is then truncated on the eastern boundary of the galaxy. The western spiral arm in the  $H\alpha$  imaging is also recognizable in this map. The SFR drops abruptly in the external disc



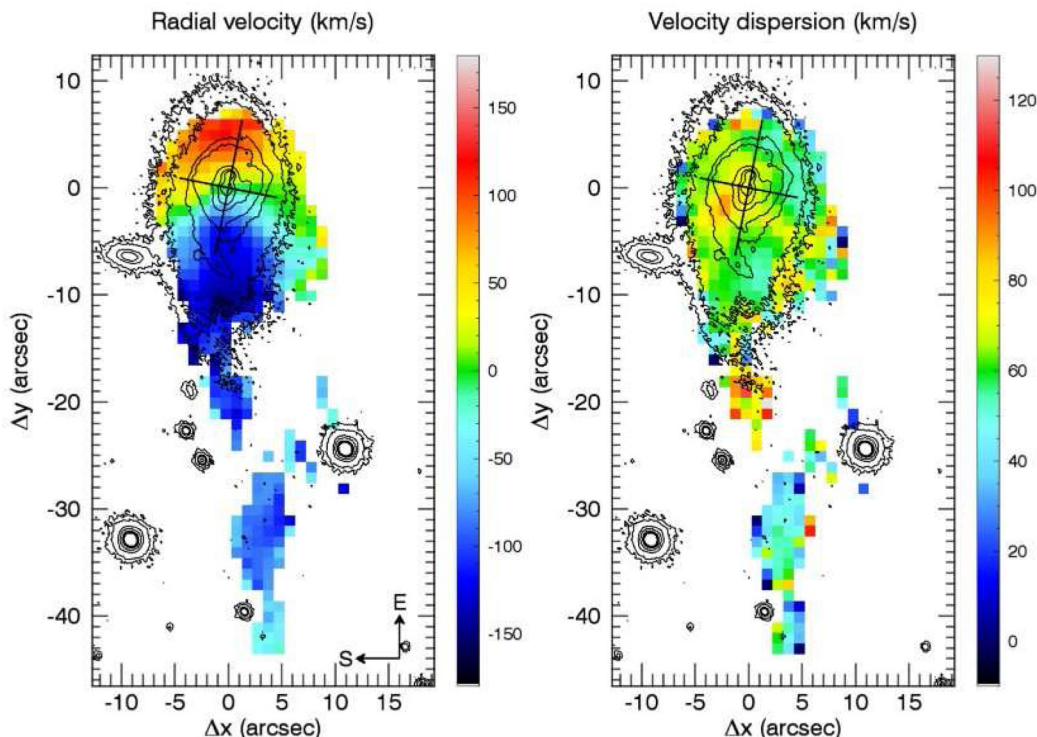


**Figure 18.** *SOS 90630*. Gas velocity fields derived from the fit to the  $H\alpha$  emission line. Left: radial velocity field. Right: velocity dispersion. Symbols as in Fig. 11.

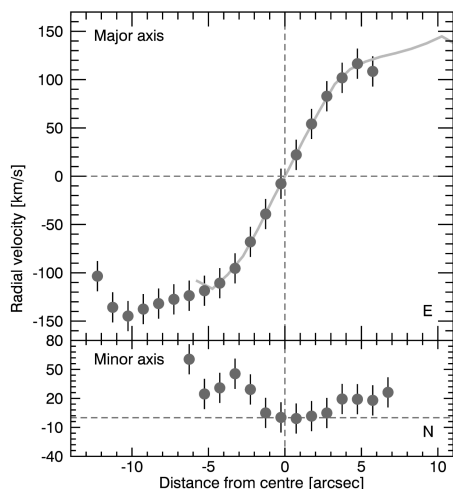


**Figure 19.** *SOS 90630*. Gas radial velocity profiles along the main axes. The grey curve in the top panel is the flipped profile plotted to assess its symmetry.

and is low in the tail. The integrated  $H\alpha$ -derived SFR of *SOS 90630* (adopting the Kroupa IMF) amounts to  $3.49 \pm 1.07 M_{\odot} \text{ yr}^{-1}$  where the error is estimated as for *SOS 61086*. The integrated  $H\alpha$ -derived SFR is consistent within the errors with that derived from UV and IR data (see Table 1).

The stellar continuum from the centre of *SOS 90630* appears relatively flat from data gathered in the blue arm of WiFeS (Fig. 9, upper panel), with 45 per cent of the integrated emission at  $4000 \text{ \AA}$  coming from stars formed less than 1 Gyr ago (thin blue curve),

while the remainder comes from an old ( $> 1$  Gyr) stellar component. This older component appears primarily due to intermediate-age stars (1.5–3 Gyr old) with little contribution from stars formed at  $z > 1$ . The young stellar component primarily consists of a single burst of SF extending over the last 200 Myr, contributing 4 per cent of the stellar mass. This is still ongoing as manifest by the strong  $H\alpha$  emission with  $\text{EW}(H\alpha) = 63 \text{ \AA}$  and other Balmer emission lines visible up to  $H\zeta$ . This relatively mild recent increase in SF is also supported by the  $\text{Ca II}$  index of 0.81 and  $H\delta/\text{Fe I } \lambda 4045$  index of 0.76, both higher than those seen in *SOS 61086*, and consistent with a 0.3 Gyr burst of SF contributing 40 per cent of the integrated light at  $4000 \text{ \AA}$  (cf. fig. 3 a of Leonardi & Rose 1996). The stellar mass contribution of recently formed stars ( $< 200$  Myr old) increases slightly to 6 per cent along the eastern edge, as does the strength of the  $H\alpha$  emission.

### 7.5 Excitation and metallicity of the gas

The BPT diagrams for *SOS 90630* present no evidence that shocks play a role in the excitation of the gas within the main body of the galaxy, or within its extended tail. Indeed, the sequence of observed points in Fig. 23 indicates that the excitation is due to  $H II$  regions with a fair range of abundance values. This abundance range is caused by the fact that this galaxy has a clearly defined abundance gradient, as can be seen in Fig. 24, where the individual abundances are again derived using PYTHON module PYQZ described in Dopita et al. (2013). Also for this galaxy, the ionization parameter spans a narrow ( $\sigma_{\log q} = 0.08$ ) range of values around  $\log q = 7.02$ . The tail of the galaxy shows appreciably lower oxygen abundance than the main body, identifying this gas as having come from the outer regions of the galaxy.

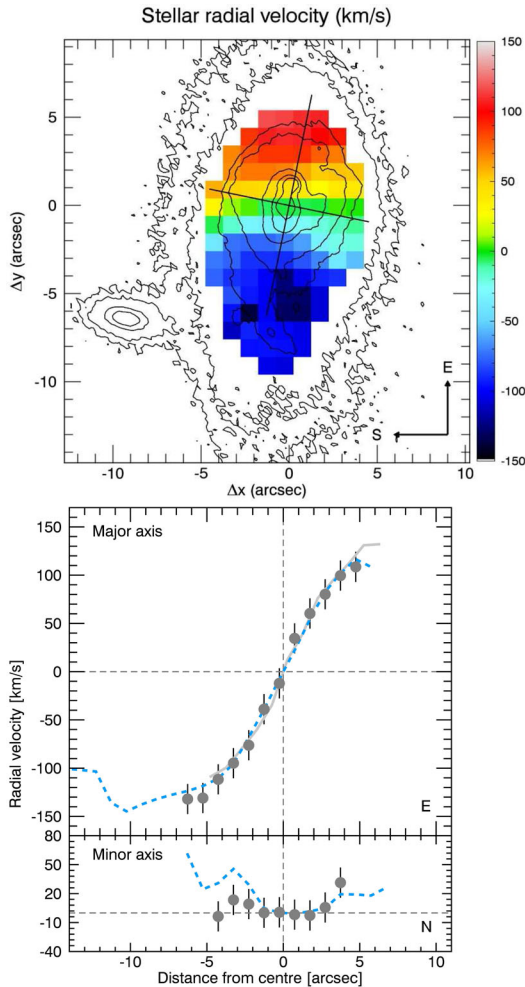


**Figure 20.** *SOS 90630*. Stellar velocity field (top) with stellar radial velocity profiles (grey dots) compared with the gas one (cyan dashed line, bottom).

## 8 DISCUSSION

*SOS 61086* and *SOS 90630* are characterized by extraplanar ionized gas extending out to projected distances of 30 and 41 kpc, respectively. Such tails have been observed in other cluster galaxies (e.g. Vollmer, Huchtmeier & van Driel 2005a; Sun, Donahue & Voit 2007; Yagi et al. 2007, 2010; Yoshida et al. 2012; Boselli et al. 2016), but their origin is not easy to determine since different possible causes, acting at different epochs, may contribute to the observed features. Such large-scale outflows of gas from a galactic disc may be due to TI or RPS. We aim to investigate which of these mechanisms dominates the evolution of the two galaxies although the solution may not be unique.

Both galaxies have other supercluster members in their proximity which could potentially interact with them. The best candidates for TI with *SOS 61086* and *SOS 90630* are *SOS 61087* and *SOS 90090*, respectively.

### 8.1 *SOS 61086*

The ‘companion’ of *SOS 61086* is an early-type galaxy located at a distance of  $\sim 17$  kpc in projection and  $\sim 300$  km s $^{-1}$  in LOS velocity from *SOS 61086*. The difference in redshift is lower than the velocity dispersion of the host cluster SC 1329–313. Since the two galaxies have comparable masses, a possible interaction could

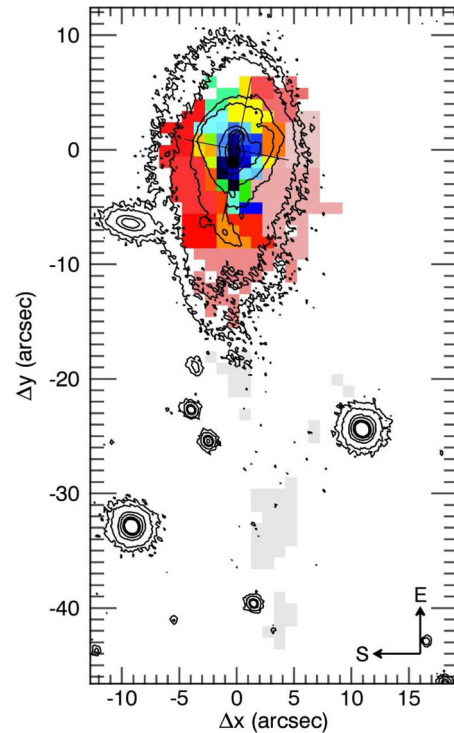


**Figure 21.** *SOS 90630*. The 48 galaxy regions identified by the WVT are shown in different colours, which are consistently used in Fig. 23.

strongly affect their structures and SFs and may induce gas/star outflow. However, we do not observe any clear disturbance in the stellar disc of *SOS 61086* and *SOS 61087* is a ‘red and dead’ galaxy without any signs of perturbation.

The gas from the outer disc of *SOS 61086* has almost all been removed from the outer edge of the disc beyond 7–8 kpc from the centre, and all that is left is the denser ISM close to the nucleus and that associated with the inner disc. The truncated gas disc and the fan shape of the extraplanar gas point to ongoing RPS. The gas tail expands to the north in the direction of the possible companion galaxy, but it extends more than 10 kpc further in projection beyond *SOS 61087* in such a way that it cannot be a bridge between the two galaxies. We already noticed that the rotational component of the gas disc is preserved in the extraplanar material (at least up to 12 kpc from the disc) as seen in other cases of galaxies subjected to ram pressure (e.g. Merluzzi et al. 2013; Fumagalli et al. 2014). No tidal stripping scenario would be able to preserve such a rotational signature in this way, while RPS acting almost face-on could provide a natural explanation.

The gas velocity profile is asymmetric as foreseen in galaxies affected by RPS and TI (Kronberger et al. 2008, 2006), but a comparison of the gas and stellar velocity profiles shows that the two components are clearly decoupled with the gas having lower velocities on average and the stellar profile being fairly symmetric. This strongly favours the RPS hypothesis.

The peak of luminosity in the centre is dominated by a young population ( $< 1$  Gyr) of stars indicative of a recent/ongoing starburst. This feature can be associated with RPS as shown by simulations (Kapferer et al. 2009; Steinhauser et al. 2012) and observations (Merluzzi et al. 2013; Yagi et al. 2013; Kenney et al. 2014). Crowl & Kenney (2008) conducted a survey of 10 Virgo galaxies with SparsePak IFS. They found clear evidence of RPS-induced SF within the truncation radius and a passive population beyond it.

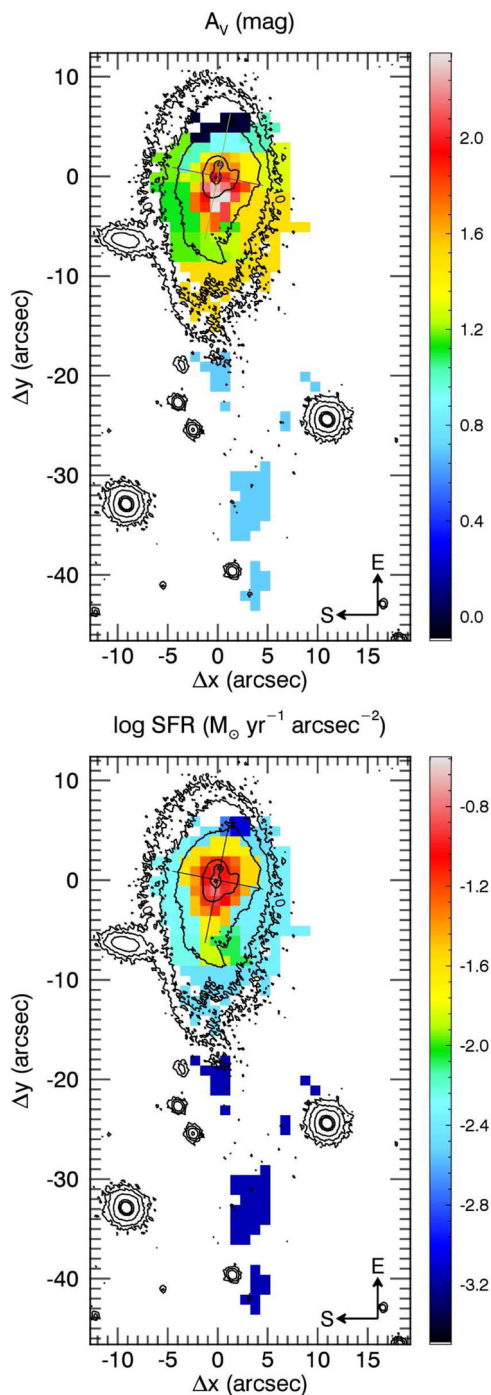


**Figure 22.** *SOS 90630*. Dust attenuation derived from the  $H\alpha/H\beta$  line ratio (top) and attenuation-corrected SFR (bottom). The inset in the top panel is a zoom of the central region of the galaxy (see the text).

A burst of SF can also be induced by TI (e.g. Kronberger et al. 2006), but would take place close to the pericentre passage (e.g. Di Matteo et al. 2008), where the galaxies are heavily perturbed, and this is not our case. The top panel of Fig. 10 shows  $H\alpha$  emission knots well out of the disc and also this feature can be related to both RPS and TI. With respect to the source of excitation, differently to other galaxies affected by ram pressure, here shocks are not important: the line ratios are characteristics of  $H II$  regions across the galaxy

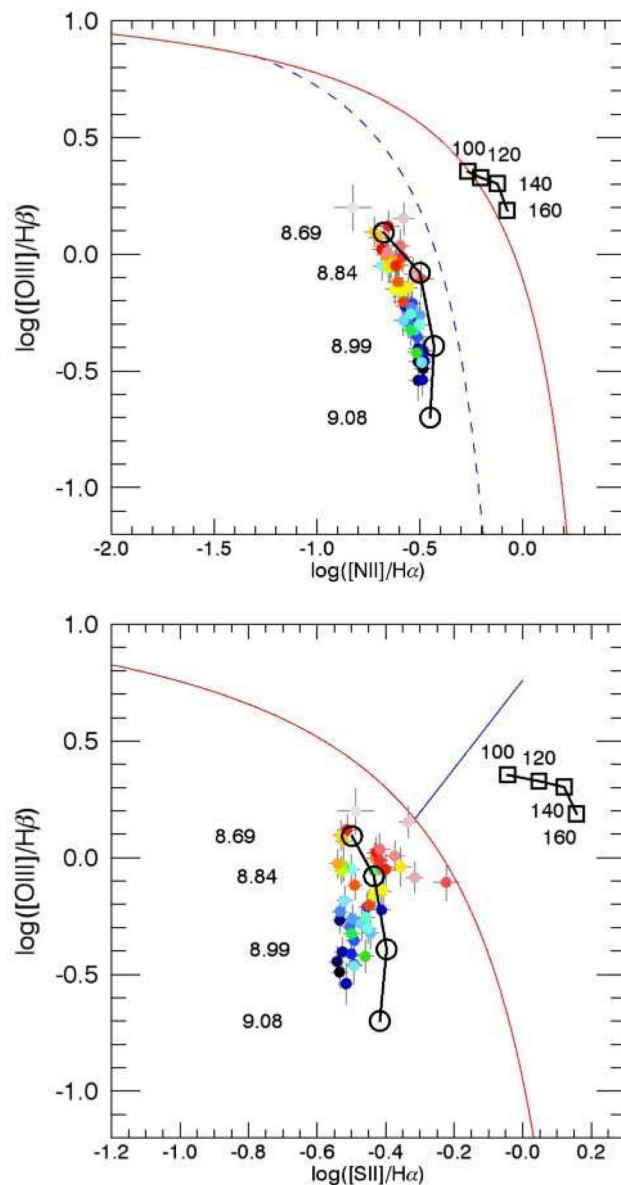


**Figure 23.** *SOS 90630*. Line flux diagnostic diagrams for the different regions of *SOS 90630*. Colours code the galaxy regions shown in Fig. 21. Other symbols like in Fig. 15.

and in the tail, except for one region in the NE tail. This is not the case in other galaxies showing RPS such as NGC 4330, NGC 4402, NGC 4501, NGC 4522 (Wong et al. 2014) and NGC 4569 (Boselli et al. 2016) in the Virgo cluster, IC 4040 (Yoshida et al. 2012) in the Coma cluster, ESO137–001 (Fossati et al. 2016) in the Norma cluster and *SOS 114372* (Merluzzi et al. 2013) in the cluster A3558. Nevertheless, our observations suggest that SF is occurring in the tail which is also inferred, for instance, by Yagi et al. (2013) for NGC 4388 in the Virgo cluster and Fumagalli et al. (2014) for ESO137–001 in the Norma cluster.

In summary, the pieces of observational evidence support in general the RPS scenario, although we cannot exclude a TI in a very early phase. We investigate if RPS alone can explain the observed gas kinematics running  $N$ -body/hydrodynamical simulations of RPS for *SOS 61086*.



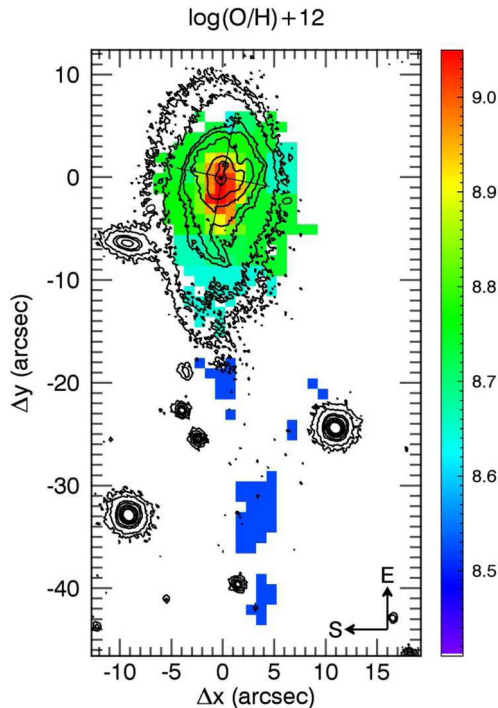


**Figure 24.** *SOS 90630*. The O/H abundance ratios derived using the *PYQZ* module.

## 8.2 *SOS 90630*

*SOS 90630* is distant 68 kpc in projection and  $\sim 320$  km s $^{-1}$  in LOS velocity from *SOS 90090* and the two galaxies belong to SC 1327–312 which has a velocity dispersion of 535 km s $^{-1}$ . The tail of extraplanar gas is directed towards the other galaxy (see Fig. 17), which, incidentally, is a factor of 4–5 more massive.

The SF across *SOS 90630* is highly asymmetric (upper panel of Fig. 17 and lower panel of Fig. 22) with a ‘crown’ of H I regions tracing the eastern disc and other star-forming regions in the western disc elongated towards the tail in a spiral arm. A single burst of SF over the last 200 Myr and still ongoing is responsible for the young stellar population detected in the centre (Section 7.4). What induced this burst and the asymmetric SF across the disc?

The gas and stellar velocity profiles coincide in the inner disc, but are decoupled in the outer disc along the minor axis. Along the major axis, we observed the gas truncation in the leading eastern edge and the gas tail leading west following the galaxy rotation with an inversion only in the more distant section. In the case of RPS, this would be acting almost edge-on to reproduce the shape of the outflowing gas. The gas emission is consistent with photoionization throughout the galaxy and in the tail.

The crown of H $\alpha$  emission evokes the decoupled dust clouds observed in two Virgo spirals by Abramson & Kenney (2014). They show the bulk of the dust being pushed back into the galaxy by ram pressure, leaving behind a population of isolated giant molecular clouds located up to 1.5 kpc beyond the edge of the main dust lane. These molecular clouds are the only parts of the ISM currently able to resist the ram pressure which is acting to decouple them from the rest of the lower density ISM material. Similar features are also observed by Yagi et al. (2013) in NGC 4388. This is confirmed in the present case by the low dust extinction measured in the leading edge and increasing towards the galaxy centre and in the western galaxy disc (see Fig. 22). We notice however that similar features

are also found in hydrodynamical simulations of mergers (Teyssier, Chapon & Bournaud 2010) where the gas response to the interaction is dominated by fragmentation in dense clouds along the spiral arms.

The observational evidence alone does not allow us to establish which mechanism prevails over the other. While the truncation of the gas disc supports the RPS, other indicators as the *r*-band imaging tend to TI between *SOS 90630* and the close massive *SOS 90090* although its disc does not present obvious signs of perturbations. This reminds us about the case of NGC 4438 in the Virgo cluster with a stellar tidal tail and extraplanar gas (Vollmer et al. 2005b); its companion NGC 4435 presents an almost regular disc in the optical image. We chose to run solely hydrodynamical simulations of RPS even in this case for two main reasons. First, our aim is to investigate if RPS can play any role and at what extent. Secondly, to set the hydrodynamical simulations of TI would imply to make assumptions on the impact parameters, the spatial trajectories and the relative velocities of the galaxies, which are almost impossible to constrain, and therefore render the results of such simulations very uncertain.

## 8.3 Ram-pressure stripping

The effects of RPS depend on the properties of both the galaxy and the ICM as well as the relative velocity. For the galaxies, we adopt the parameters listed in Table 1 and Section 2. The ram pressure is given by  $P_{\text{ram}} = \rho_{\text{ICM}} V^2$ , where  $\rho_{\text{ICM}}$  is the density of the ICM and  $V$  is the velocity of the galaxy relative to the ICM. These parameters are estimated as follows.

### 8.3.1 ICM densities

Successive *XMM-Newton* observations have now continuously covered the SSCC filament that connects A3562, SC 1329–313, SC 1329–312 and A3558. Out of these observations, photon-event light curves have been analysed in order to filter any flare contamination, i.e. observation periods with an anomalous count rate. This ‘cleaning’ procedure yields 11 filtered event lists that we re-processed using the *XMM-Newton* Science Analysis System (*SAS*) version 14.0.0 in order to select the relevant calibration files. Following a procedure described in Bourdin & Mazzotta (2008), the filtered event lists have been re-binned in sky coordinate and energy, and associated with both a 3D effective exposure and a background noise model. As detailed in Bourdin et al. (2013), the background noise model includes astrophysical and instrumental components that have been jointly fitted within a sky area that excludes the brightest region of each cluster. A wavelet denoised image of the SSCC filament derived from this data set is shown in Fig. 1. Assuming that the ICM is spherically symmetric in the innermost regions of SC 1329–313 and SC 1329–312, we deprojected a couple of gas density profiles centred on each cluster peak. To do so, analytic profiles of the gas density and temperature (Vikhlinin et al. 2006) were projected along the LOS following the weighting scheme proposed by Mazzotta et al. (2004), and fitted to the radially averaged surface brightness and spectroscopic temperature. In this procedure, the ICM emissivity is modelled following the Astrophysical Plasma Emission Code (Smith et al. 2001), shifted to  $z = 0.049$  and absorbed assuming a Galactic hydrogen density column of  $N_{\text{H}} = 3.96 \times 10^{20}$  cm $^{-2}$ . The derived profiles are shown in Fig. 25.

*SOS 61086* and *SOS 90630* are located at 282 and 226 kpc, respectively, in projection from the X-ray cluster centres. Interpolating the density profiles at these radii, we obtain electron densities

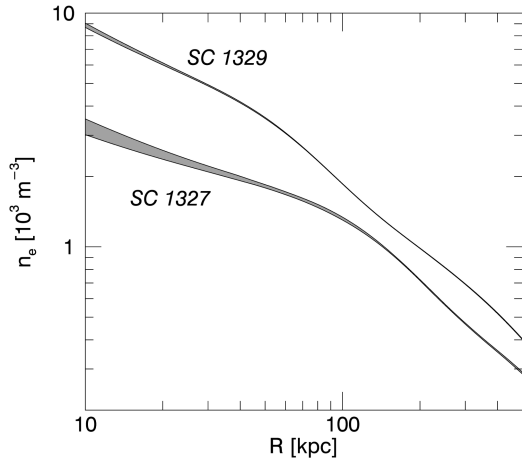


**Figure 25.** Electronic density profiles centred on the X-ray surface brightness peaks of the galaxy clusters, SC 1329–313 and SC 1329–312 (see the text).

$n_e$  of  $\sim 5 \times 10^{-4}$  and  $\sim 9 \times 10^{-4} \text{ cm}^{-3}$ , respectively. Assuming a metallicity of  $Z=0.3 Z_\odot$  and the element abundances of Grevesse & Sauval (1998), the particle mean weight per hydrogen atom is  $\mu_H = 1.34732$ , and the number of electrons per hydrogen atom is  $\nu_H = 1.17366$ . Given these values, the ICM mass density can be derived from the electronic density:

$$\rho_{\text{ICM}} = \frac{\mu_H m_p}{\nu_H} n_e.$$

Therefore, electronic densities measured for SOS 61086 and SOS 90630, at the projected distances, translate in gas mass densities of  $\rho_{\text{ICM}}(\text{SOS 61086}) \simeq 9.6 \times 10^{-28} \text{ g cm}^{-3}$  and  $\rho_{\text{ICM}}(\text{SOS 90630}) \simeq 1.7 \times 10^{-27} \text{ g cm}^{-3}$ . However, these are upper limits since if the galaxies are at larger 3D distances, their local densities will be lower. We account for this possibility considering also lower values for the ICM densities. At about  $2\times$  the projected radius, we measure  $\rho_{\text{ICM}}(\text{SOS 61086}) \simeq 5.5 \times 10^{-28} \text{ g cm}^{-3}$  and  $\rho_{\text{ICM}}(\text{SOS 90630}) \simeq 7.7 \times 10^{-28} \text{ g cm}^{-3}$ .

### 8.3.2 Orbital velocities of the galaxies

As lower limits for the orbital velocities, we assume the galaxies' LOS velocities relative to the clusters' systemic velocities  $V_{\text{los, SOS 61086}} \sim -612 \text{ km s}^{-1}$  and  $V_{\text{los, SOS 90630}} \sim -336 \text{ km s}^{-1}$  (both galaxies have lower velocities with respect to the systemic ones, indicating that they are moving towards the observer). The galaxies have also a velocity component in the plane of the sky, as suggested by the geometry of the gas tails. For the upper limits to the spatial velocity, we assume a velocity equal to  $3\times$  the cluster velocity dispersion, i.e. 1000 and  $1500 \text{ km s}^{-1}$  for SOS 61086 and SOS 90630, respectively.

The inclination of the galaxy disc and the distribution of the extraplanar gas suggest that the RPS is acting almost face-on on SOS 61086 and almost edge-on on SOS 90630. The inclination angle  $\beta$  between the galaxy rotation axis and the ICM wind direction has been shown to influence the amount of the gas pushed out of the disc in the first phase of the stripping, only in the case of moderate ram pressure (e.g. Marcolini et al. 2003; Roediger & Hensler 2005). On the other hand,  $\beta$  can be important in drawing the shape of the stripped gas. We note that in the observed shape another factor is crucial, i.e. the position of the observer with respect to both the wind and the galaxy disc.

For SOS 61086, there is an indication that the galaxy is not moving radially into the cluster: the extraplanar gas extends N-S while the cluster centre is located west of the galaxy position projected in the sky. We explored the values in the ranges: 500–1000 and 500–1500  $\text{km s}^{-1}$  for the orbital velocity of SOS 61086 and SOS 90630, respectively. For the inclination angle, we considered a wide range  $0^\circ \leq \beta \leq 80^\circ$ . Our approach was to run low-resolution simulations for a grid of parameters and then select the most promising cases for the high-resolution simulations.

### 8.3.3 Constraints on RPS

To check if the expected ram pressure is able to strip the gas from the disc of SOS 61086 and SOS 90630, we compare it to the gravitational restoring force per unit area  $(d\phi/dz)\Sigma_{\text{gas}} = 2\pi G \Sigma_{\text{star}} \Sigma_{\text{gas}}$ , with  $\Sigma_{\text{star}}$  and  $\Sigma_{\text{gas}}$  the star and gas surface density, respectively (e.g. Kenney, van Gorkom & Vollmer 2004; Domainko et al. 2006). The stellar mass surface density in the disc is given by  $\Sigma_{\text{star}}(r) = \Sigma_{\text{star}}(0) \times \exp(-r/r_d)$ , where  $r_d$  is the disc scale radius and  $\Sigma_{\text{star}}(0) = \mathcal{M}_d/(2\pi r_d^2)$  with  $\mathcal{M}_d$  the mass of the disc. The disc scale radii are  $r_d = 2.86$  and  $2.05 \text{ kpc}$  for SOS 61086 and SOS 90630, respectively.<sup>8</sup>

The mass surface density at the stripping radius,  $r_{\text{strip}}$ , is  $\Sigma_{\text{star}}(r_{\text{strip}}) = \Sigma_{\text{star}}(0) \times \exp(-r_{\text{strip}}/r_d)$ . The ram pressure is equal to the restoring force at radius  $r_{\text{strip}}$  when  $\rho_{\text{ICM}} V^2 = 2\pi G \Sigma_{\text{star}}(0) \times \exp(-r_{\text{strip}}/r_d) \Sigma_{\text{gas}}$ . We assume a typical  $\Sigma_{\text{gas}} \sim 10 \text{ M}_\odot \text{ pc}^{-2}$  (e.g. Kenney et al. 2004). For SOS 61086 we have  $\mathcal{M}_d = 2.8 \times 10^9 \text{ M}_\odot$ ,  $r_d = 2.9 \text{ kpc}$ ,  $r_{\text{strip}} = 6.2 \text{ kpc}$  so the ram pressure can be effective in removing the gas from the disc if  $V \geq 350 \text{ km s}^{-1}$  and  $V \geq 470 \text{ km s}^{-1}$  with high and low density of the ICM (see Section 8.3.1). For SOS 90630, we have  $\mathcal{M}_d = 9.5 \times 10^9 \text{ M}_\odot$ ,  $r_d = 2.0 \text{ kpc}$ ,  $r_{\text{strip}} = 6.1 \text{ kpc}$  implying  $V \geq 450 \text{ km s}^{-1}$  and  $V \geq 650 \text{ km s}^{-1}$  for high and low density of the ICM (see Section 8.3.1). In these estimates, we assumed the ram pressure acting face-on but simulations show that the inclination angle does not play a major role unless the ram pressure is acting very close to edge-on (Roediger & Brüggén 2006).

Combining the ICM density estimates and the velocity ranges for the two galaxies, the ram pressure ranges from  $\sim 1.4 \times 10^{-12}$  to  $\sim 9.6 \times 10^{-12} \text{ dyn cm}^{-2}$  for SOS 61086 and from  $\sim 1.9 \times 10^{-12}$  to  $\sim 3.8 \times 10^{-11} \text{ dyn cm}^{-2}$  for SOS 90630. Following Roediger & Hensler (2005), these are the regimes of weak to moderate ram pressure for SOS 61086 and moderate to high ram pressure for SOS 90630. Their 2D hydrodynamical simulations demonstrated that ram-pressure effects can be observed over a wide range of ICM conditions and even in low-density environments, such as cluster outskirts and poor clusters as in this case, where the moderate ram pressure can bend the gaseous disc of  $L^*$  galaxies. Taking into account that our galaxies are 2.7–2.1 mag fainter than  $L^*$ , we expect the ram pressure being much more efficient up to determining the truncation of the gas disc, as we observe (e.g. Marcolini et al. 2003).

## 9 DOES RPS EXPLAIN THE OBSERVATIONS?

The main goal of the simulations is to understand to what extent ram pressure might explain the main observed features of the gas: the truncation of the disc, the shape and extension of the tail and the

<sup>8</sup> These quantities were derived by fitting the VISTA  $K$ -band images using GALFIT (Peng et al. 2010) and corrected for dust absorption following Graham & Worley (2008).

**Table 2.** Set-up of the simulations. Initial properties of the two galaxy models. First, the parameters of the modified NFW (Di Cintio et al. 2014a) haloes: concentration  $c$ ; shape parameters  $\alpha$ ,  $\beta$ ,  $\gamma$ ; scale radius  $r_s$ ; scale density  $\rho_s$ . Afterwards the setting for disc and bulge, following Springel et al. (2005).  $v_{200}$  is the velocity at the virial radius  $r_{200}$ ,  $\lambda$  the dimensionless spin parameter. The disc and bulge mass fractions are  $m_d$  and  $m_b$ , with  $f_{\text{gas}}$  being the initial gas amount in the disc and  $z_0$  giving the disc height as a fraction of the disc scale length  $r_d$ .

	SOS 61086	SOS 90630
$c$	9.619	9.165
$\alpha$	1.556	1.071
$\beta$	2.691	2.797
$\gamma$	0.7897	0.993
$r_s$ (kpc)	7.91	9.08
$\rho_s$ ( $M_\odot \text{ yr}^{-1}$ )	$0.705 \times 10^7$	$1.161 \times 10^7$
$v_{200}$ ( $\text{km s}^{-1}$ )	93	120
$\lambda$	0.033	0.033
$m_d$	0.0285	0.0355
$m_b$	0.003 92	0.003 69
$f_{\text{gas}}$	0.48	0.24
$z_0$	0.2	0.2
$r_d$ (kpc)	2.61	2.05

kinematics. This would eventually constrain the ICM wind angle and velocity and the time of the onset (‘age’) of RPS.

### 9.1 N-body/hydrodynamical simulations of RPS

We performed simulations of model galaxies resembling SOS 61086 and SOS 90630 and experiencing RPS. The simulations have been done with the cosmological moving-mesh code AREPO (Springel 2010). Contrary to ordinary grid codes, the Euler equations of ideal hydrodynamics are solved on a moving mesh which allows us to construct a Galilean-invariant scheme. Such an approach allows an accurate treatment of gas mixing and fluid instabilities (Rayleigh–Taylor or Kelvin–Helmholtz instabilities), both crucial in RPS simulations. In the simulations, radiative cooling (Katz, Weinberg & Hernquist 1996) and a sub-grid, multi-phase model for SF and stellar feedback (Springel & Hernquist 2003) are included as well.

To simulate a galaxy undergoing RPS, we use a wind-tunnel set-up similar to Heß & Springel (2012). First, model galaxies are generated, resembling pre-interaction properties of SOS 61086 and SOS 90630. Initial conditions for an exponential stellar and gaseous disc, as well as a stellar bulge with a Hernquist (1990) profile, of those model galaxies are calculated according to Springel, Di Matteo & Hernquist (2005), based on theoretical work by Mo, Mao & White (1998). For the dark-matter halo, we are using a modified NFW profile according to Di Cintio et al. (2014a), and also include a hot gas halo. The properties of the model galaxies are shown in Table 2. Those model galaxies are put into a cuboidal simulation domain with extension  $200 \times 100 \times 100 \text{ kpc}^3$  with the model galaxy statically placed at (50, 50, 50) kpc. The dark-matter halo is represented by a static gravitational potential, yielding an additional force on stellar particles and gas cells in addition to their self-gravity.

RPS is simulated by imposing a wind on the model galaxies. To this extent, gas cells are inserted in front of the galaxy with the preferred density, velocity and a constant volume of 4 or  $40 \text{ kpc}^3$ , depending on the resolution of the simulation. When they pass by the galaxy, the resolution is adjusted and gas cells are refined in

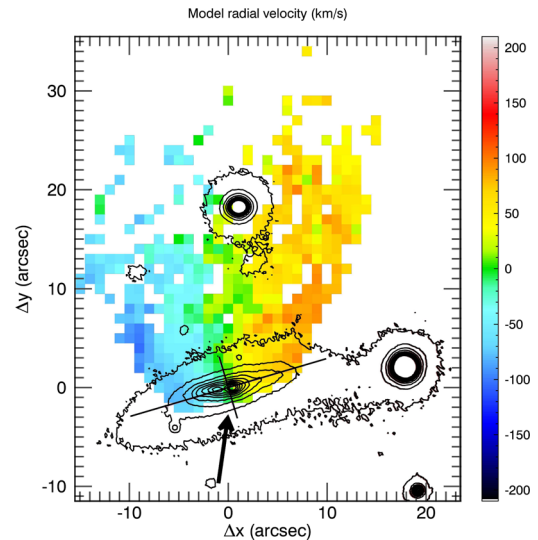


**Figure 26.** *SOS 61086*. The best model ( $\beta = 30^\circ$ ,  $V_{\text{wind}} = 750 \text{ km s}^{-1}$  and  $t = 250 \text{ Myr}$ ) of the simulated gas velocity field with superimposed the  $r$ -band isophotes (dark-red). The projected wind direction is indicated by the white arrow. This figure should be compared with Fig. 11.

order to avoid too large volume discrepancies of neighbouring cells. Furthermore, the mass resolution of gas cells which mainly contain ISM is kept at a constant value in order to produce stellar particles with a constant mass. At the end of the simulation domain, all gas cells are removed. To distinguish between gas cells containing either ICM or ISM, a colouring technique as described in e.g. Vogelsberger et al. (2012) is used. Gravitational softening lengths are set according to Hayward et al. (2014). We are using  $2 \times 10^5$  particles/cells for the stellar and gaseous disc, respectively, as well as  $5 \times 10^4$  particles for the stellar bulge. On average, the wind tunnel contains  $4.5 \times 10^5$  gas cells. For the low-resolution runs (LR), we use a 10th of the particles/cells.

The models were run from the onset of the ram pressure to 1 Gyr after and stored in steps of 10 Myr. During this time, the ram pressure is kept constant and its onset is immediate.

### 9.2 Simulations analysis

The simulations were run in the ranges of wind velocity and inclination angle defined in Section 8.3.2. To compare the results of simulations to the observed velocity fields, we proceeded as outlined in Merluzzi et al. (2013) and summarized below. We first oriented the models with respect to the observer in such a way that their LOS velocity equals the observed velocity relative to the parent cluster. Then, we integrated the velocities of the individual cells along the LOS and binned the derived velocity fields in square pixels of 1 arcsec side, to simulate our IFS data. In doing this, we only considered cells whose fraction of disc gas is greater than a certain threshold to minimize the bias on the velocity field coming from ICM particles. We adopted a threshold of 0.5, although the results remain constant for a relatively wide range (0.2–0.9) of this parameter. A visual comparison of the data and the models then leads to the selection of the parameters of the best RPS models.

In Fig. 26, we show the simulation which better matches the gas velocity field of SOS 61086 and the projection on the plane of the sky of the ICM wind direction. This model corresponds to  $\beta = 30^\circ$ ,



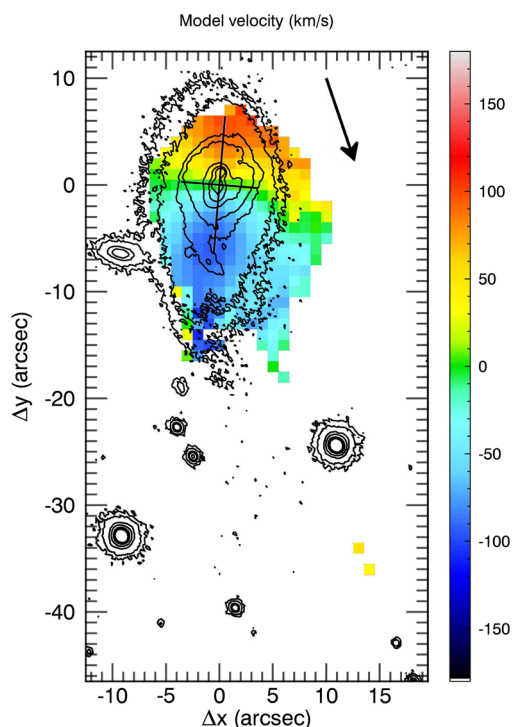


**Figure 27.** *SOS 90630*. The best model ( $\beta = 80^\circ$ ,  $V_{\text{wind}} = 500 \text{ km s}^{-1}$  and  $t = 120 \text{ Myr}$ ) of the simulated gas velocity field with superimposed the  $r$ -band isophotes (dark-red). The projected wind direction is indicated by the white arrow. This figure should be compared with Fig. 18.

$V_{\text{wind}} = 750 \text{ km s}^{-1}$ ,  $t = 250 \text{ Myr}$  and  $\rho_{\text{ICM}} \simeq 5.5 \times 10^{-28} \text{ g cm}^{-3}$ . We notice an overall agreement between the model and the WiFeS observations (Fig. 11, top panel). Both the velocity range and the gas distribution are well reproduced by the model, where the gas extends further in projection with respect to *SOS 61087*. Nevertheless, two particular features cannot be reproduced by any models: the presence of the ionized gas in the central south disc and the blueshifted gas clumps observed in the furthest extraplanar gas.

The neutral and ionized gas are assumed to be mixed as suggested by simulations and observations (Tonnesen & Bryan 2010; Abramson et al. 2011), but in principle the simulations show the velocity field of the whole gas, while our data refer to the ionized gas. This can be the origin of discrepancies between models and observations. In particular, the ionized gas in the south disc may be due to a galactic wind or the presence of denser clouds more resilient to the ram pressure. The blueshifted furthest clumps of gas detected by WiFeS suggest a scenario where the disc screens off the detached gas which, being still bound, falls back into the disc. Such a complicated configuration is difficult to be reproduced by the simulations.

In the case of *SOS 90630*, we obtained the best match for  $\beta = 80^\circ$ ,  $V_{\text{wind}} = 750 \text{ km s}^{-1}$  and  $\rho_{\text{ICM}} \simeq 7.7 \times 10^{-28} \text{ g cm}^{-3}$ , which is shown in Fig. 27 after 120 Myr from the ram-pressure onset. For this galaxy, we are not able with the simulations to reproduce both the tail in its whole extent and the observed truncation of the gas disc. When in the simulations the tail forms, the disc appears much more truncated than observed and the gas velocity field is not consistent with the observed one. Therefore, RPS alone does not seem sufficient to produce the tail, and the help of another force is needed to pull the gas tail from the disc.

Gavazzi et al. (2001) and Vollmer et al. (2005a) studied two cases in which the ram pressure was aided by TI in forming the gas tails of two galaxies in A1367 and Virgo. The role of TI is, in their cases, to loosen the restoring force of the galaxy thus making RPS more effective. *SOS 90090*, the massive galaxy close in projection to *SOS 90630*, could in principle induce such a tidal disturbance. To investigate this possibility, we estimate the acceleration  $a_{\text{tid}}$  produced by *SOS 90090* on the ISM of *SOS 90630* and compare it with the acceleration from the potential of *SOS 90630* itself,  $a_{\text{gal}}$ , following Vollmer et al. (2005a). We have

$$\frac{a_{\text{tid}}}{a_{\text{gal}}} = \frac{M_{90090}}{M_{90630}} \left( \frac{r}{R} - 1 \right)^{-2},$$

where  $R$  is the distance from the centre of *SOS 90630* and  $r$  is the distance between the galaxies (Vollmer et al. 2005a). As a proxy of the mass ratio, we use the stellar mass ratio, but of course we do not know  $r$ . In the special case in which projected and true distance coincide (both galaxies in the plane of sky), the above equation would imply that the tidal force begins to dominate over the restoring force at  $R > 18 \text{ kpc}$ , which is the projected distance where the gas tail begins. At three disc scale radii ( $R \sim 8.5 \text{ kpc}$ ), the above ratio is 0.17, which shows that the tidal force might be able to produce some perturbation also in the disc, as is possibly observed in the structure of the external SE disc (see Fig. 4).

This is a very crude approach, however, since (i) it is most probable that the distance between the galaxies is larger; (ii) the above formula is just a rough approximation; and (iii) we definitely lack the knowledge of the orbits of the two galaxies (e.g. they might have been closer in the past). On the other hand, in the light of the cases quoted above, TI does not need to be the only or dominant mechanism to produce the tail, but only strong enough to ‘help’ the ram pressure, and this might well be the case unless the two galaxies are very distant in space. We finally notice that the direction of the gas tail is intermediate between the direction of the wind in the RPS simulation and the direction of *SOS 90090*, which could point to a collaborative role of the two mechanisms.

We can therefore conclude that the phenomenology of the ionized gas is explained in part by the ram-pressure acting close to edge-on and pushing the gas in the NW direction. For what concerns the tail, we can only argue that TI with *SOS 90090* could have acted as an aid to the RPS.

The crown of star-forming regions suggests ram-pressure-induced SF due to the gas compression at the leading edge where the gas disc is truncated and the dust seems to be swept out. In fact, the age of the RPS is consistent with the burst of SF, started 200 Myr ago and still ongoing. Star-forming regions in the tail, foreseen in the simulations, are inferred by the  $\text{H}\alpha$  knots detected up to 40 kpc from the disc in the narrow-band imaging. However, our data do not allow us to determine if these clumps origin from newly formed stars or stars stripped from the disc by the possible combined action of RPS and TI.

### 9.3 The role of cluster–cluster interaction

The dynamical analysis (Bardelli et al. 1994, 1998a) and diffuse filamentary X-ray emission (Bardelli et al. 1996; Hanami et al. 1999; Kull & Böhringer 1999) showed that the five clusters of the SSCC are interacting with recent and/or ongoing cluster–cluster mergers.

Finoguenov et al. (2004) proposed a TI between SC 1329–313 and A3562 to explain the observed properties of the hot gas in A3562 – the tailed shape of the X-ray emission associated with

SC 1329–313 as well as the sloshing of the A3562 core. In their scenario, SC 1329–313 was initially flying north of A3562 in the western direction and after passage at pericentre with A3562 deflected south. This is also suggested by the X-ray structure of SC 1329–313 (see Fig. 1). Radio observations confirmed this scenario (Giacintucci et al. 2005). The western extension of the radio halo in A3562 and the direction of the emission of J1332–3146a, a radio galaxy 150 kpc NE of SOS 61086 in projection, support the idea that merger-induced turbulence is present in the region between the centre of A3562 and SC 1329–313. We further remark that the fan-shape tail radio emission of J1332–3146a follows the same direction of the outflowing ionized gas of SOS 61086, which is also a radio source. This particular similarity in shape and orientation between the two tails, although having different origins, may witness for the first time that cluster interactions trigger RPS events by perturbing the ICM.

SOS 90630 is member of SC 1327–312 which also may have interacted with A3558 (e.g. Rossetti et al. 2007), but in this case an RPS event alone cannot explain the observations and another mechanism such as TI should be considered. It is interesting to notice that this galaxy can be easily identified as a *jellyfish* galaxy, i.e. the ‘perfect’ candidate of ongoing RPS.

## 10 SUMMARY AND FINAL REMARKS

The present study investigates the ongoing transformations of two low-mass galaxies in poor cluster environments with the aim of understanding which are the mechanisms responsible. SOS 61086 and SOS 90630 have been selected from deep subarcsec-resolution imaging as promising candidates of ongoing gas stripping. Both have a possible companion which may also suggest a TI. We notice that this can often be the case in dense cluster environments, complicating the identification of ongoing RPS events.

From the analysis of multi-band data and IFS observations complemented by ad hoc hydrodynamical simulations, we come to envision the following scenarios.

*SOS 61086.* The ionized gas distribution (truncated disc, 30 kpc tail) and velocity field together with the properties of the stellar component (unperturbed morphology and velocity field) support the RPS scenario. Star-forming regions are found in the central disc, but also in the outflowing gas, as foreseen in case of RPS (Roediger et al. 2014). In fact, the gas turns out to be mainly photoionized throughout the galaxy and its tail. The dust is pushed by ram pressure, with the leading edge showing much lower attenuation.

Although some of these features can be suggestive also of TI, the hydrodynamical simulations of RPS well reproduce the overall gas velocity field with  $\beta = 80^\circ$ ,  $V_{\text{wind}} = 750 \text{ km s}^{-1}$  and  $t = 250 \text{ Myr}$ . It is encouraging that the time of the onset of ram pressure agrees with the age of the young stellar populations ( $\sim 200 \text{ Myr}$ ). As in SOS 114372 (Merluzzi et al. 2013), we are very likely observing ram-pressure-induced SF. All this supports a scenario where ongoing RPS is the dominant mechanism at work.

*SOS 90630.* The most distinctive features of this galaxy are the very long (41 kpc) tail of ionized gas and the truncated gaseous disc. The attenuation is lower on the leading edge of the disc and SF could be present in the tail. In this case, the ram pressure explains the truncation of the gas disc, which is consistent with the distribution of dust and SF, while RPS and TI with SOS 90090 are responsible for the long gas tail.

We notice that both galaxies are members of interacting clusters, suggesting that these systems can trigger RPS events by perturbing the ICM. Finally, this work provides another clear proof that RPS

can take place in very different environments from cluster cores to cluster outskirts, from rich clusters to poor ones, affecting in various ways galaxies of different masses.

### 10.1 Final remarks

All simulations of RPS indicate that it should be very efficient in quenching SF of cluster galaxies, but its effects depend on ICM and ISM properties, which may easily change locally, as well as on the galaxy orbits. All together these parameters contribute to determine case-by-case what fraction of gas is stripped from the galaxy and over what time-scales. In fact, there are events where the ICM–ISM interaction is not able to strip all the gaseous reservoir of a galaxy and then definitely quench its SF. Which is the impact of RPS on the evolution of cluster/group galaxies?

At present, only a few tens of ongoing RPS events have been ascertained and studied in detail; most of these galaxies belong to nearby clusters with only a few cases found in clusters at intermediate redshift (e.g. Owen et al. 2005; Cortese et al. 2007; Crowl & Kenney 2008; Vollmer et al. 2010; Yagi et al. 2010; Abramson & Kenney 2014; Wong et al. 2014; Boselli et al. 2016; Fossati et al. 2016). Thus, the identification of new cases of galaxies experiencing RPS is definitely important. One of the reasons for the small statistics is the intrinsic and observational biases such as the short time-scales and the observer’s point of view with respect to the galaxy trajectory. The latter particularly disadvantages the selection of RPS candidates based only on photometric data which allow us to recognize distorted morphology and to glimpse one-side extraplanar emission, but cannot identify other features such as the truncation of the gas disc and robust detection of extraplanar gas. In addition, this approach is not able at all to disentangle between the effects of TI and RPS, which might be similar.

Nevertheless, recently Poggianti et al. (2016) and McPartland et al. (2016) have undertaken a systematic search in two samples of nearby and intermediate-redshift clusters, respectively, using almost the same morphological criteria. They inferred that the morphologically selected galaxies are RPS candidates. Among the 13 galaxies of the Shapley supercluster observed with WiFeS because of hints of extraplanar emission from their images, 9 ( $\sim 70$  per cent) actually presented extraplanar ionized gas and only 4 ( $\sim 30$  per cent) turned out to be significantly affected by ram pressure. Thus, certain caution is needed before drawing conclusions on the basis of samples of candidates. Ebeling et al. (2014) introduced three criteria to identify RPS candidates: disturbed morphology indicative of a unilateral external force; (ii) brightness knots and colour gradients suggesting bursts of SF; (iii) evidence of tails. If we adopt the criteria of Ebeling et al. (2014) to identify RPS candidates in our spectroscopic sample of supercluster galaxies (80 per cent complete at  $m^* + 3$ ,  $i = 17.6$ ), we find that 0.5 per cent follows all the Ebeling et al.’s criteria in full agreement with the 0.6 per cent found by Ebeling et al. (2014).<sup>9</sup> If we adopt at least two of the three Ebeling et al.’s criteria and apply our success percentage of the 30 per cent, we expect to identify about 25 cases of ongoing RPS in the whole ShaSS survey (11 clusters covering  $23 \text{ deg}^2$ ) which would be a significant increase in the number of known ongoing RPS events. Although such a large number is supported by the hypothesis that RPS is triggered by cluster mergers (Owers et al. 2012), only a campaign of IFS observations

<sup>9</sup> Once accounted for the non-cluster members, i.e. 57 per cent of the selected galaxies by Ebeling et al. (2014).

(or  $H_1$  for nearby clusters) can confirm this indicative conjecture and this is the project we are carrying out with WiFeS.

## ACKNOWLEDGEMENTS

This work is based on data collected with (i) WiFeS at the 2.3 m telescope of the Australian National University at Siding Spring (Australia) and (ii) OmegaCAM at the ESO INAF-VLT Survey Telescope and VIRCAM at VISTA, both at the European Southern Observatory, Chile (ESO Programmes 088.A-4008, 089.A-0095, 090.A-0094, 091.A-0050, 093.A-0465). We thank the referee for the comments and corrections which improved the presentation of our work. We also thank Volker Springel for providing the simulation code `AREPO` and Tiziana Venturi for her help with the interpretation of the radio data. The optical imaging is collected at the VLT Survey Telescope using the Italian INAF Guaranteed Time of Observations and reduced by A. Grado and L. Limatola. CPH was funded by CONICYT Anillo project ACT-1122. PM and GB acknowledge financial support from PRIN-INAF2014: *Galaxy Evolution from Cluster Cores to Filaments* (PI: B. M. Poggianti). MAD acknowledges the support of the Australian Research Council (ARC) through Discovery Project DP130103925, and he would also like to thank the Deanship of Scientific Research (DSR), King Abdulaziz University for additional financial support as Distinguished Visiting Professor under the KAU Hi-Ci programme. DS acknowledges the support from the Austrian Federal Ministry of Science, Research and Economy as part of the UniInfrastrukturprogramm of the Focal Point Scientific Computing at the University of Innsbruck.

## REFERENCES

- Abadi M. G., Moore B., Bower R. G., 1999, *MNRAS*, 308, 947  
Abramson A., Kenney J. D. P., 2014, *AJ*, 147, 63  
Abramson A., Kenney J. D. P., Crowl H. H., Chung A., van Gorkom J. H., Vollmer B., Schiminovich D., 2011, *AJ*, 141, 164  
Baes M. et al., 2003, *MNRAS*, 343, 1081  
Bahé Y. M., McCarthy I. G., Balogh M. L., Font A. S., 2013, *MNRAS*, 430, 3017  
Baldwin J. A., Phillips M. M., Terlevich R., 1981, *PASP*, 93, 5  
Bamford S. P. et al., 2009, *MNRAS*, 393, 1324  
Bardelli S., Zucca E., Vettolani G., Zamorani G., Scaramella R., Collin C. A., MacGillivray H. T., 1994, *MNRAS*, 267, 665  
Bardelli S., Zucca E., Malizia A., Zamorani G., Scaramella R., Vettolani G., 1996, *A&A*, 305, 435  
Bardelli S., Zucca E., Zamorani G., Vettolani G., Scaramella R., 1998a, *MNRAS*, 296, 599  
Bardelli S., Pisani A., Ramella M., Zucca E., Zamorani G., 1998b, *MNRAS*, 300, 589  
Barnes J. E., Hernquist L. E., 1991, *ApJ*, 370, L65  
Barnes J. E., Hernquist L., 1992, *ARA&A*, 30, 705  
Barnes J. E., Hernquist L., 1996, *ApJ*, 471, 115  
Bekki K., 2001, *ApJ*, 546, 189  
Bekki K., 2014, *MNRAS*, 438, 444  
Boselli A., Gavazzi G., 2006, *PASP*, 118, 517  
Boselli A. et al., 2016, *A&A*, 587, A68  
Bourdin H., Mazzotta P., 2008, *A&A*, 479, 307  
Bourdin H., Mazzotta P., Markevitch M., Giacintucci S., Brunetti G., 2013, *ApJ*, 764, 82  
Bournaud F., Duc P.-A., Amram P., Combes F., Gach J.-L., 2004, *A&A*, 425, 813  
Byrd G., Valtonen M., 1990, *ApJ*, 350, 89  
Cardelli J. A., Clayton G. C., Mathis J. S., 1989, *ApJ*, 345, 245  
Christlein D., Zabludoff A. I., 2004, *ApJ*, 616, 192  
Chung A., van Gorkom J. H., Kenney J. D. P., Vollmer B., 2007, *ApJ*, 659, L115  
Chung A., van Gorkom J. H., Kenney J. D. P., Crowl H., Vollmer B., 2009, *AJ*, 138, 1741  
Cortese L. et al., 2007, *MNRAS*, 376, 157  
Cowie L. L., Songalia A., 1977, *Nature*, 266, 501  
Crowl H. H., Kenney J. D. P., 2008, *AJ*, 136, 1623  
Di Cintio A., Brook C. B., Dutton A. A., Stinson S., Knebe A., 2014a, *MNRAS*, 10, 1  
Di Cintio A., Brook C. B., Dutton A. A., Macciò A. V., Stinson G. S., Knebe A., 2014b, *MNRAS*, 441, 2986  
Di Matteo P., Bournaud F., Martig M., Combes F., Melchior A.-L., Semelin B., 2008, *A&A*, 492, 31  
Diehl S., Statler T. S., 2006, *MNRAS*, 368, 497  
Domainko W. et al., 2006, *A&A*, 452, 795  
Dopita M., Hart J., McGregor P., Oates P., Bloxham G., Jones D., 2007, *Ap&SS*, 310, 255  
Dopita M. et al., 2010, *Ap&SS*, 327, 245  
Dopita M. A., Sutherland R. S., Nicholls D. C., Kewley L. J., Vogt F. P. A., 2013, *ApJS*, 208, 10  
Dressler A., 1980, *ApJ*, 236, 351  
Ebeling H., Stephenson L. N., Edge A. C., 2014, *ApJ*, 781, L40  
Finoguenov A., Henriksen M. J., Briel U. G., de Plaa J., Kaastra J. S., 2004, *ApJ*, 611, 811  
Fischera J., Dopita M., 2005, *ApJ*, 619, 340  
Fossati M., Fumagalli M., Boselli A., Gavazzi G., Sun M., Wilman D. J., 2016, *MNRAS*, 455, 2028  
Fujita Y., Nagashima M., 1999, *ApJ*, 516, 619  
Fumagalli M., Fossati M., Hau G. K. T., Gavazzi G., Bower R., Sun M., Boselli A., 2014, *MNRAS*, 445, 4335  
Gavazzi G., Boselli A., Mayer L., Iglesias-Paramo J., Vilchez J. M., Carrasco L., 2001, *ApJ*, 563, L23  
Giacintucci S. et al., 2005, *A&A*, 440, 867  
Giovanelli R., Haynes M. P., 2002, *ApJ*, 571, L107  
Graham A. W., Worley C. C., 2008, *MNRAS*, 388, 1708  
Grevesse N., Sauval A. J., 1998, *Space Sci. Rev.*, 85, 161  
Gunn J. E., Gott J. R. I., 1972, *ApJ*, 176, 1  
Haines C. P., Merluzzi P., Mercurio A., Gargiulo A., Krusanova N., Busarello G., La Barbera F., Capaccioli M., 2006, *MNRAS*, 371, 55  
Haines C. P., Busarello G., Merluzzi P., Smith R. J., Raychaudhury S., Mercurio A., Smith G. P., 2011, *MNRAS*, 412, 127  
Hanami H., Tsuru T., Shimasaku K., Yamauchi S., Ikebe Y., Koyama K., 1999, *ApJ*, 521, 90  
Hayward C. C., Torrey P., Springel V., Hernquist L., Vogelsberger M., 2014, *MNRAS*, 442, 1992  
Hernquist L., 1990, *ApJ*, 356, 359  
Heß S., Springel V., 2012, *MNRAS*, 426, 3112  
James P. A., Prescott M., Baldry I. K., 2008, *A&A*, 484, 703  
Kapferer W., Sluka C., Schindler S., Ferrari C., Ziegler B., 2009, *A&A*, 499, 87  
Katz N., Weinberg D. H., Hernquist L., 1996, *ApJ*, 105, 19  
Kauffmann G. et al., 2003, *MNRAS*, 346, 1055  
Keel W. C., Kennicutt R. C., Jr, Hummel E., van der Hulst J. M., 1985, *AJ*, 90, 708  
Kenney J. D. P., van Gorkom J. H., Vollmer B., 2004, *AJ*, 127, 3361  
Kenney J. D. P., Geha M., Jáchym P., Crowl H. H., Dague W., Chung A., van Gorkom J., Vollmer B., 2014, *ApJ*, 780, 119  
Kennicutt R. C., Jr, 1983, *ApJ*, 272, 54  
Kennicutt R. C., Jr, 1998, *ApJ*, 498, 541  
Kennicutt R. C., Jr, Keel W. C., 1984, *ApJ*, 279, L5  
Kennicutt R. C., Jr, Tamblyn P., Congdon C. E., 1994, *ApJ*, 435, 22  
Kewley L. J., Heisler C. A., Dopita M. A., Lumsden S., 2001, *ApJS*, 132, 37  
Kewley L. J., Groves B., Kauffmann G., Heckman T., 2006, *MNRAS*, 372, 961  
Kormendy J., Bender R., 2012, *ApJS*, 198, 2  
Kregel M., van der Kruit P. C., Freeman K. C., 2004, *MNRAS*, 351, 1247



Kronberger T., Kapferer W., Schindler S., Böhm A., Kutdemir E., Ziegler B. L., 2006, *A&A*, 458, 69

Kronberger T., Kapferer W., Unterguggenberger S., Schindler S., Ziegler B. L., 2008, *A&A*, 483, 783

Kroupa P., 2001, *MNRAS*, 322, 231

Kull A., Böhringer H., 1999, *A&A*, 341, 23

Larson R. B., Tinsley B. M., 1978, *ApJ*, 219, 46

Larson R. B., Tinsley B. M., Caldwell C. M., 1980, *ApJ*, 237, 692

Leonardi A. J., Rose J. A., 1996, *AJ*, 111, 182

Lewis I. et al., 2002, *MNRAS*, 334, 673

McPartland C., Ebeling H., Roediger E., Blumenthal K., 2016, *MNRAS*, 455, 2994

Marcolini A., Brighenti F., D’Ercole A., 2003, *MNRAS*, 345, 1329

Mazzotta P., Rasia E., Moscardini L., Tormen G., 2004, *MNRAS*, 354, 10

Mercurio A. et al., 2006, *MNRAS*, 368, 109

Mercurio A. et al., 2015, *MNRAS*, 453, 3685

Merluzzi P., Mercurio A., Haines C. P., Smith R. J., Busarello G., Lucey J. R., 2010, *MNRAS*, 402, 753

Merluzzi P. et al., 2013, *MNRAS*, 429, 1747

Merluzzi P. et al., 2015, *MNRAS*, 446, 803

Miller N. A., 2005, *AJ*, 130, 2541

Mo H. J., Mao S., White S. D. M., 1998, *MNRAS*, 295, 319

Moore B., Katz N., Lake G., Dressler A., Oemler A., 1996, *Nature*, 379, 613

Moran S. M., Miller N., Treu T., Ellis R. S., Smith G. P., 2007, *ApJ*, 659, 1138

Nulsen P. E. J., 1982, *MNRAS*, 192, 1007

Oh S. H., Kim W.-T., Lee H. M., Kim J., 2008, *ApJ*, 683, 94

Owen F. N., Ledlow M. J., Keel W. C., Wang Q. D., Morrison G. E., 2005, *AJ*, 129, 31

Owers M. S., Couch W. J., Nulsen P. E. J., Randall S. W., 2012, *ApJ*, 750, L23

Peng C. Y., Ho L. C., Impey C. D., Rix H.-W., 2010, *AJ*, 139, 2097

Poggianti B. M. et al., 2016, *AJ*, 151, 78

Ragone C. J., Muriel H., Proust D., Reisenegger A., Quintana H., 2006, *A&A*, 445, 819

Roediger E., Brüggem M., 2006, *MNRAS*, 369, 567

Roediger E., Hensler G., 2005, *A&A*, 433, 875

Roediger E., Brüggem M., Owers M. S., Ebeling H., Sun M., 2014, *MNRAS*, 443, L114

Rose J. A., 1985, *AJ*, 90, 1927

Rossetti M., Ghizzardi S., Molendi S., Finoguenov A., 2007, *A&A*, 463, 839

Sánchez-Blázquez P. et al., 2006, *MNRAS*, 371, 703

Schlaflly E. F., Finkbeiner D. P., 2011, *ApJ*, 737, 103

Schlegel D. J., Finkbeiner D. P., Davis M., 1998, *ApJ*, 500, 525

Smith R. K., Brickhouse N. S., Liedahl D. A., Raymond J. C., 2001, *ApJ*, 556, L91

Springel V., 2010, *MNRAS*, 401, 791

Springel V., Hernquist L., 2003, *MNRAS*, 339, 289

Springel V., Di Matteo T., Hernquist L., 2005, *MNRAS*, 361, 776

Steinhauser D., Haider M., Kapferer W., Schindler S., 2012, *A&A*, 544, A54

Sun M., Donahue M., Voit G. M., 2007, *ApJ*, 671, 190

Taylor E. N. et al., 2011, *MNRAS*, 418, 1587

Teyssier R., Chapon D., Bournaud F., 2010, *ApJ*, 720, L149

Tonnesen S., Bryan G. L., 2010, *ApJ*, 709, 1203

Tonnesen S., Bryan G. L., 2012, *MNRAS*, 422, 1609

Toomre A., Toomre J., 1972, *ApJ*, 178, 623

Valotto C., Giovanelli R., 2004, *AJ*, 128, 115

Vazdekis A., Sánchez-Blázquez P., Falcón-Barroso J., Cenarro A. J., Beasley M. A., Cardiel N., Gorgas J., Peletier R. F., 2010, *MNRAS*, 404, 1639

Veilleux S., Osterbrock D. E., 1987, *ApJS*, 63, 295

Veilleux S., Bland-Hawthorn J., Cecil G., Tully R. B., Miller S. T., 1999, *ApJ*, 520, 111

Veilleux S. et al., 2010, *AJ*, 139, 145

Vikhlinin A., Kravtsov A., Forman W., Jones C., Markevitch M., Murray S. S., Van Speybroeck L., 2006, *ApJ*, 640, 691

Vogelsberger M., Sijacki D., Kereš D., Springel V., Hernquist L., 2012, *MNRAS*, 425, 3024

Vollmer B., Huchtmeier W., van Driel W., 2005a, *A&A*, 439, 921

Vollmer B., Braine J., Combes F., Sofue Y., 2005b, *A&A*, 441, 473

Vollmer B., Soida M., Chung A., Beck R., Urbanik M., Chyży K. T., Otmianowska-Mazur K., van Gorkom J. H., 2010, *A&A*, 512, 36

Williams B. F. et al., 2011, *ApJ*, 734, L22

Wong O. I., Kenney J. D. P., Murphy E. J., Helou G., 2014, *ApJ*, 783, 109

Woods D. F., Geller M. J., Barton E. J., 2006, *AJ*, 132, 197

Yagi M., Komiyama Y., Yoshida M., Furusawa H., Kashikawa N., Koyama Y., Okamura S., 2007, *ApJ*, 660, 1209

Yagi M. et al., 2010, *AJ*, 140, 1814

Yagi M., Gu L., Fujita Y., Nakazawa K., Akahori T., Hattori T., Yoshida M., Makishima K., 2013, *ApJ*, 778, 91

Yoshida M., Yagi M., Komiyama Y., Furusawa H., Kashikawa N., Hattori T., Okamura S., 2012, *ApJ*, 749, 43

## APPENDIX A: THE ORIGIN OF THE DOUBLE PEAK OF LUMINOSITY IN SOS 90630

The optical (*gri*) images of SOS 90630 in Fig. 4 present two peaks of luminosity in the centre suggesting the presence of two nuclei which are not distinguishable in the *K*-band image. To understand whether this might originate from dust absorption, we downgraded the *r*-band image (FWHM=0.64 arcsec, 0.21 arcsec pixel<sup>-1</sup>) to mimic the resolution and sampling in the *K* band (FWHM = 1.1 arcsec, 0.339 arcsec pixel<sup>-1</sup>).

Fig. A1 shows the surface brightness (SB) profiles along a line joining the two maxima in the *r* band (incidentally, this line coincides with the apparent major axis in the *K*-band image of the galaxy). The green curve is the original profile in the *r* band, the blue curve is the profile in the same band after downgrading, and the red curve is the *K*-band profile. All profiles are arbitrarily normalized to the maximum in the *K* band. It is clear that even with the

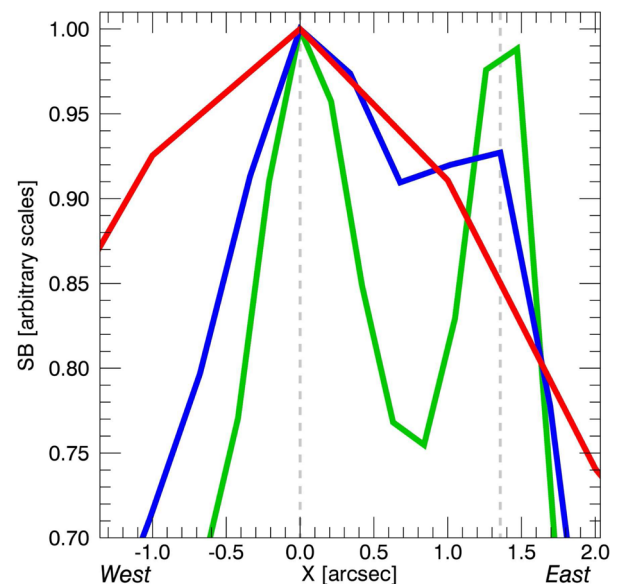


**Figure A1.** Surface brightness (SB) profiles along the major axis of SOS 90630 in the region of the two optical ‘nuclei’. The profiles in the *r* and *K* bands are shown in green and red, respectively. The blue curve is the profile of the *r*-band image after downgrading to the resolution and sampling of the *K* band. The vertical dashed lines mark the positions of the two optical ‘nuclei’. The profiles are scaled in SB to match in correspondence of the *K*-band (true) nucleus.

downgraded resolution the separation of the two ‘nuclei’ persists in the  $r$ -band profile, while in the  $K$  band there is instead only one clear maximum with a fairly symmetric distribution around it. The minimum of the  $r$ -band SB is located about 0.75 arcsec east from the nucleus. To explain the different profiles between optical and NIR, we should also assume that the western side (left in the figure)

is more dust attenuated than the eastern one. In Section 7.3, we show that this is the case. We therefore conclude that the appearance of a ‘double nucleus’ is caused by dust absorption.

This paper has been typeset from a  $\text{\TeX}/\text{\LaTeX}$  file prepared by the author.